Detection and characterization of symmetry-broken long-range orders in the spin-$\frac{1}{2}$ triangular Heisenberg model

S. N. Saadatmand* and I. P. McCulloch
ARC Centre of Excellence for Engineered Quantum Systems, School of Mathematics and Physics, The University of Queensland, St Lucia, QLD 4072, Australia
(Received 24 May 2017; published 9 August 2017)

We present new numerical tools to analyze symmetry-broken phases in the context of SU(2)-symmetric translation-invariant matrix product states (MPS) and density-matrix renormalization-group (DMRG) methods for infinite cylinders, and determine the phase diagram of the geometrically frustrated triangular Heisenberg model with nearest- and next-nearest-neighbor (NN and NNN) interactions. The appearance of Nambu-Goldstone modes in the excitation spectrum is characterized by "tower of states" levels in the momentum-resolved entanglement spectrum. Symmetry-breaking phase transitions are detected by a combination of the correlation lengths and second and fourth cumulants of the magnetic order parameters (which we call the Binder ratio), even though symmetry implies that the order parameter itself is strictly zero. Using this approach, we have identified a 120° order, a columnar order, and an algebraic spin liquid (specific to width-6 systems), alongside the previously studied topological spin liquid phase. For the latter, we also demonstrate robustness against chiral perturbations.

DOI: 10.1103/PhysRevB.96.075117

I. INTRODUCTION

The ground state of the one-dimensional nearest-neighbor Heisenberg model (originally determined in an important work by Heisenberg [1]), $H_{\mathrm{NN}} = J\sum_i \mathbf{S}_i \cdot \mathbf{S}_{i+1}$, for $J < 0$, exhibits long-range ferromagnetic (FM) order, which breaks the spins' rotational symmetry [the SU(2) group] and elementary excitations are spin-waves (also known as Nambu-Goldstone bosons or magnons; see, for example, Refs. [2–4]). The Bethe *Ansatz* [5] can be employed (e.g., see Ref. [6]) to study the antiferromagnet (AFM) spin-$\frac{1}{2}$ Heisenberg model, $J > 0$, which demonstrates the absence of magnetic ordering in clear contrast to the FM case. Today, we know there exist *no* continuous-symmetry-broken long-range order (LRO) in any one-dimensional system. In fact, magnetism in 1D and few-leg ladders is peculiarly different to higher dimensions (where LROs exist; see below), since the magnetic ordering at zero temperature is suppressed by quantum fluctuations due to the same mechanism as described by Mermin-Wagner-Hohenberg theorem for finite temperatures [7,8] (i.e., due to the low cost of creating quantum long-range fluctuations, which increases the entropy). In contrast to 1D, long-range magnetic ordering is possible in 2D Heisenberg-type Hamiltonians; early examples arose from studying anisotropy [9], the AFM Heisenberg model with $S = \frac{1}{2}$ [10–15], $S \geqslant \frac{3}{2}$ [16], large-S values [10], and for the antiferromagnetic XY [11,17] and XXZ [18,19] models for all spin magnitudes. For the majority of two-dimensional magnetic materials, if there exist *no* frustration, the ground state exhibits [4,20,21] either ferromagnetism or antiferromagnetism (i.e., the well-known bipartite Néel order [22]). It is widely believed that the celebrated Landau symmetry-breaking theorem [23,24] explains the physics behind all such conventional magnetic ordering: Hamiltonians such as H_{NN} contain a set of symmetries which are absent in the ground state, a feature known as spontaneous symmetry breaking (SSB). As a result of symmetry breaking, a well-defined order parameter exists in the model that can be used to characterize the magnetic ordering, unambiguously. After uncovering the key mechanisms behind the conventional ordering (in particular, ferromagnetism and bipartite antiferromagnetism), the field of low-dimensional quantum magnetism enjoyed a new boost of attention aimed at understanding exotic phases of quantum matter that appear in frustrated one-dimensional [3,25–30] and two-dimensional [20,21,31–33] systems. This happened partly due to the rise of the geometrically frustrated antiferromagnets on nonbipartite Archimedean lattices [2,4,20,21,34,35]. Interestingly, the existence of geometrical frustration is enough by itself to often lead to the "melting" of the magnetic ordering, stabilizing a family of nonmagnetic phases, collectively classified as *spin liquids* (also known as paramagnetic states) [31,32,36–40]. Such quantum liquids preserve all Hamiltonian symmetries and, consequently, their existence cannot be understood through Landau's symmetry-breaking paradigm. The search for new, hidden order parameters has been challenging theorists for the last 20 years, and has led to the discovery of even more intriguing phases of the quantum matter. A canonical example is the discovery of the *topological order* [32,40,41], such as symmetry-protected topological (SPT) ordering (including the Haldane phase and the Affleck-Kennedy-Lieb-Tasaki ground state [42,43]) and the intrinsic topological states [32,38] (including the Z_2-gauge ground state of the toric code [44–46]), which can only exist in $D \geqslant 2$.

Magnetic ordering is often identified using the scaling behavior of a static two-point (or higher order) correlation function. For a spin system, a two-point correlator can be written in terms of the (principal) correlation length ξ as $|G_2(i,i')| = \langle \mathbf{S}_i \cdot \mathbf{S}_{i'} \rangle \sim C + e^{-\frac{r_{ii'}}{\xi}} + \cdots$, where C stands for a constant (which can be zero), $r_{ii'}$ is the distance between sites, and ellipses represent faster decaying terms. Different type of ordering can be defined as follows. For magnetically disordered states, with no conventional order parameter (i.e., no broken symmetry), the correlation function decays to zero exponentially fast, C is zero, ξ is finite, and there is a bulk gap in the excitation spectrum. In this case, instead of symmetry breaking, we have *symmetry protection*, giving rise to the SPT

*nariman.saadatmand@uq.edu.au

order. Such an exponential drop is observed in the Haldane phase (as an example, see the original calculations by White and Huse [47]). For true LROs, such as Néel-type AFMs and the FM state with a conventional order parameter, the correlation function tends to a constant at large distances, $\xi \to \infty$. There exists another distinct long-range phase of the quantum matter, which is referred to as a quantum critical state (or a quasi-LRO). In such phases, the correlation function decays with a *power law* with distance. Power-law decaying correlation functions can be approximated as the sum of many exponential functions, as occurs in the MPS *Ansatz* [48,49], which again translates to having diverging ξ, consistent with the Bethe *Ansatz*' prediction for the spin-$\frac{1}{2}$ Heisenberg chain. Critical states are common in 1D quantum magnetism and appear at a transition between two gapped disordered phases with different symmetries, when the gap necessarily closes; however, they can also stabilize in an extended region, as in the *XY phase* of the anisotropic Heisenberg chain [2,4].

High-accuracy numerical methods, such as exact diagonalization (ED), quantum Monte Carlo (QMC), (see Ref. [50] for a review), and coupled cluster [21] methods, are often used for low-temperature frustrated magnets, modeled as strongly interacting spin Hamiltonians exhibiting many-sublattice ground states. In this paper, we employ and expand the functionality of the finite DMRG (fDMRG) [51–54], and the state-of-the-art infinite DMRG (iDMRG) [54,55] methods to characterize LROs of a geometrically frustrated system, when the many-body states are constructed through the SU(2)-symmetric (non-Abelian) MPS and infinite MPS (iMPS) *Ansätze* [53–56], respectively. The latter is a translation-invariant MPS that allows the calculation of many useful quantities directly in the thermodynamic limit via transfer matrix methods. Currently, there exist few well-established numerical tools, in the context of nonsymmetric DMRG, to identify LROs. In finite-system MPS studies, SSB needs to be treated carefully because in exact calculations SSB does not occur at all [20,57], as finite size effects induce a gap between states that would be degenerate in the thermodynamic limit. In practice, with finite-precision arithmetic symmetry breaking can occur when the finite-size gap is smaller than the characteristic energy scale set by the accuracy of the numerics (in MPS calculations, this is set by the energy scale associated with the basis truncation). This can be difficult to control, as symmetry breaking might occur as a side effect of the numerical algorithm or it might require an additional perturbation. Infinite-size MPS (or very large finite MPS) are better behaved in this respect, where there are a variety of techniques; one can look at the scaling of the correlation length of the ground state against MPS number of states, m, which distinguishes gapped and gapless states [55,58,59], direct measurement of local magnetization order parameters, the entanglement entropy [60], and the static spin structure factor (SSF, see below). However, when the Hamiltonian symmetries are preserved explicitly, the order parameter is zero by construction and a robust set of numerical tools for characterizing magnetic ordering is not readily available. Here, we introduce and verify the accuracy of two new numerical tools, in the context of SU(2)-symmetric iMPS/iDMRG, to characterize and locate phase transitions incorporating LROs in the triangular Heisenberg model (THM) on infinite cylinders. New tools include the study of the cumulants (cf. Ref. [61] for the definitions and relevant discussions on the noncentral moments and the cumulants in the context of the probability theory) and a Binder ratio of magnetization order parameters, and further developments on tower-of-states (TOS) level patterns in the momentum-resolved entanglement spectra (ES) [62–64].

The triangular lattice has the highest geometrical frustration in the Archimedean crystal family with a coordination number of $Z_c = 6$. Anderson and Fazekas [65,66] argued that the high frustration of the triangular lattice might be enough to melt the long-range magnetic ordering observed for the Heisenberg model on the square lattice (e.g., see Refs. [4,20,21]). In the first work, Anderson conjectured that the spin-$\frac{1}{2}$ THM with antiferromagnetic NN bonds should stabilize a resonating-valance-bond (RVB) ground state (i.e., the equally weighted superposition of all possible arrangements of the singlet dimers on the lattice; RVBs are the building blocks of the quantum liquids). The failure of robust analytical and numerical studies to find an RVB ground state motivates the search for a minimal extension to $H_{\rm NN}$ that increases the frustration. The obvious choice is frustration through the addition of a NNN coupling term, which frustrates the 120°-ordered arrangement of sublattices (see below and Refs. [12,21,67–78]). This led to the introduction of the J_1-J_2 THM, for which the Hamiltonian is defined as

$$H_{J_2} = J_1 \sum_{\langle i,j \rangle} \mathbf{S}_i \cdot \mathbf{S}_j + J_2 \sum_{\langle\langle i,j \rangle\rangle} \mathbf{S}_i \cdot \mathbf{S}_j, \qquad (1)$$

where $\langle i,j \rangle$ ($\langle\langle i,j \rangle\rangle$) indicates that the sum goes over all NN (NNN) couplings. The SU(2) symmetry of H_{J_2} can be simply realized by noticing $[H_{J_2}, \mathbf{S}] = 0$ ($\mathbf{S}$ stands for the total spin vector), which means that eigenvalues of $\mathbf{S}^2$ are good quantum numbers and can be used to label ground-state symmetry sectors. Geometrical frustration forbids the bipartite Néel order as a stable ground state of the antiferromagnetic NN model ($J_1 > 0$ and $J_2 = 0$). Consequently, one expects the ground state, for the majority of the phase diagram of the antiferromagnetic H_{J_2}, to be a compromise, such as a 120°-ordered arrangement [20,21,79]. By now, it is well-known that the ground state of the nearest-neighbor THM does *not* exhibit an RVB but is instead a quasiclassical LRO 120° state, which is less stable [69,70,72,74,75] than the Néel order on the square lattice, since the sublattice magnetization of the triangular lattice is significantly reduced compared to its classical value. Because of this reduced stability, inherent to the triangular lattice, upon perturbing the Hamiltonian one may expect to see a variety of new phases. There have been some historically important semiclassical spin-wave theory (SWT) and ED studies [67,70,71,80,81] for the model. However, such studies did not cover the physics of the whole phase diagram and were not able to capture the detailed properties of the ground states. Previously, we elucidated [79] the complete phase diagram of the J_1-J_2 THM on three-leg finite- and infinite-length cylinders to understand the crossover of 1D and 2D physics in the model. Moreover, other precise numerical approaches [74–78,82–85] demonstrate the existence of a spin-liquid (SL) state that stabilizes in a region ranging from $J_2^{\rm low} \approx 0.05$ [83] up to $J_2^{\rm high} \approx 0.19$ [82]. Some numerical studies discovered magnetic orders outside this approximate SL region (see, for

example, Refs. [21,70–72,75,84]). However, we suggest the detailed properties of the magnetic ground states are still unclear in comparison to the well-understood counterparts in the (semi-)classical THM [70,71] and the quantum model on the three-leg cylinders. In particular, for the finite-size lattices, the largest system sizes for which the magnetic ordering of the J_1-J_2 THM was thoroughly studied is an 18×18 torus [74] and a 30×3 cylinder [79].

It is noteworthy that the J_1-J_2 THM can describe some low-temperature properties of quasi-2D organic lattices, such as κ-(BEDT-TTF)$_2$Cu$_2$(CN)$_3$ and Me$_3$EtP[Pd(dmit)$_2$]$_2$, and inorganic materials, such as Cs_2CuCl_4, Cs_2CuBr_4, and $RbFe(MoO_4)_2$ (see Refs. [31,33,86] for details).

In this work, we establish the phase diagram for the J_1-J_2 THM on infinite-length cylinders with width up to 12 sites and show that the model contains an LRO coplanar three-sublattice 120° order ($J_2 \leqslant 0.105(5)$), a fourfold degenerate toric-code-type Z_2-gauge spin liquid ($0.105(5) \leqslant J_2 \leqslant 0.140(5)$; see also Ref. [85]), an LRO collinear two-sublattice columnar order ($0.140(5) \leqslant J_2 \leqslant 0.170(5)$ and $0.200(5) \leqslant J_2 \leqslant 0.5$ for width-6 cylinders, and $0.140(5) \leqslant J_2 \leqslant 0.5$ for larger cylinders), and an algebraic spin liquid [40] (ASL) ground state ($0.170(5) \leqslant J_2 \leqslant 0.200(5)$, only for width-6 cylinders). The new tools for the cumulants and Binder ratios of the order parameter allowed us to locate the aforementioned phase transitions accurately, while the patterns of the TOS levels in the momentum-resolved ES revealed the structure of the magnetic order (or its absence). We also consider the explicit breaking of the time-reversal symmetry in the J_1-J_2 THM and the possibility of the stabilization of a chiral LRO. We note that there were recent, indecisive discussions [84,85,87] on the robustness of the topological spin liquids against perturbing H_{J_2} with a chiral term. Here, we confirm the nonchiral nature of such ground states and the existence of a continuous phase transition toward the chiral spin liquid [36,37,40] (CSL) phase through the study of a scalar chiral order parameter on width-8 cylinders.

The rest of the paper is organized as follows. In Sec. II, we provide the details of the employed SU(2)-symmetric MPS and DMRG methods (in particular, how we construct order parameter operators) and the geometry of the cylindrical lattices (in particular, the MPS mapping). In Sec. III, we present an overview of each of the phases, a schematic phase diagram for the model, and a more quantitative diagram in the form of short-range correlations. In Sec. IV, we directly measure the magnetization order parameters on some small-width ($L_y = 3,4,5,6$) finite-length cylinders using MPS/fDMRG algorithms, to benchmark our calculations with another algorithm. Afterward, we focus on presenting our more precise iMPS/iDMRG results on infinite cylinders (having widths up to $L_y^{\max} = 12$). In Sec. V, we investigate the scaling behaviors of the correlation lengths against m, deep in each phase region. In Sec. VI, in order to better understand the entanglement entropy of the symmetry-broken LROs on cylinders, we study the entropy in the columnar magnetically ordered phase. Details of our numerical tools are presented in Secs. VII and VIII, for cumulants and Binder ratios of the magnetization order parameters, and for TOS levels in the momentum-resolved ES, respectively. In Sec. IX, we test the robustness of a topological SL ground state against chiral perturbations of the Hamiltonian to investigate the formation of long-range chiral ordering, before some concluding remarks in Sec. X.

II. METHODS

To obtain the variational ground state of the THM for a wide range of FM and AFM J_2 values in Eq. (1), we set $J_1 = 1$ as the unit of the energy, and employ the single-site DMRG algorithm (incorporating density-matrix mixing [88] with subspace expansion [89] and SU(2) symmetry [53,90]). In addition, we construct the operators using the efficient formalism of matrix product operators [53–55,91] (MPOs), which represents an operator analogous to an ordinary MPS matrix. The MPO structure provides a formulation of any polynomial operator (with an expectation value that scales polynomially with the size of the lattice) in a Schur form (an upper- or lower-triangular matrix) for infinite systems [55,92] (see below for an example and also Ref. [93] for an overview), which allows the calculation of the asymptotic limit of the expectation value per site. We keep up to $m = 2\,000$ number of states [approximately equivalent to 6 000 states of an Abelian U(1)-symmetric basis] in MPS/fDMRG, and up to $m = 3\,000$ number of states [approximately 9 000 U(1) states] in iMPS/iDMRG calculations. Due to inherent 1D nature of the MPS, a mapping between the *Ansatz* wave function and the triangular lattice is necessary. For the mapping purposes, we wrap the lattice in a way to create a long (or infinite-length) $L_x \times L_y$-site cylinder (L_x can go to infinity; we also set $L = L_x \times L_y$) as in Fig. 1. We will employ a standard notation, previously presented in Ref. [79] (originally developed for single-wall carbon nano-tubes [94]), to specify the wrapping vectors of the cylinders, $\mathbf{C}_0$, in terms of principal lattice directions using a notation of ($\hat{\mathbf{a}}_{+60^\circ}$,$\hat{\mathbf{a}}_{-60^\circ}$). For the majority of the calculations, we choose the so-called YC wrapping, $\mathbf{C}_0[\mathrm{YC}] = (L_y, -L_y)$ (we shall use the shorthand notations of YCL_y and YC$L_x \times L_y$ to specify different YC

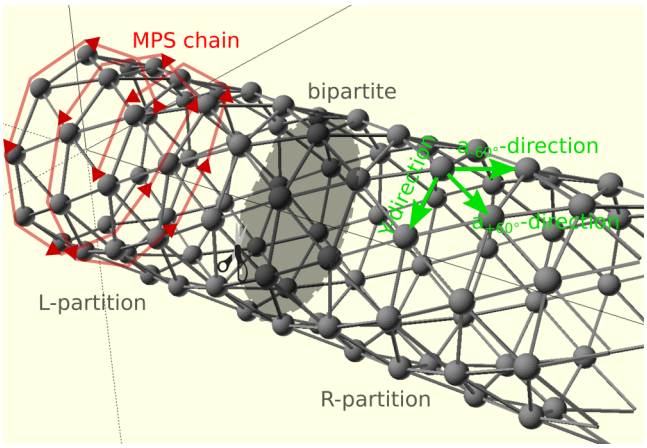

FIG. 1. Cartoon visualization of a triangular lattice on a YC cylinder. Spins sit on spheres. An "efficient" mapping of the MPS chain is shown using the red spiral. The green arrows represent the unit vectors on three principal lattice directions. The transparent gray plane corresponds to the bipartite cut that creates partitions L and R, without crossing any Y-direction bond.

lattice sizes). The YC structure is the only wrapping method with a circumference that equals to L_y (Y axis now coincides with the lattice short direction and the X axis coincides with the lattice long direction) and is the best choice for the momentum-resolved ES (see below). However, in general, the choice of L_y and $\mathbf{C}_0$ should respect the sublattice ordering (if any) of the target state to avoid frustrating the ground state. Consequently, depending on the desired width, the YC structure cannot be always used. Therefore, in finite-L_x fDMRG calculations, we use a YC6 structure in all regions (allowing the stabilization of up to tripartite-symmetric ground states), and YC3, $\mathbf{C}_0[L_y = 4] = (4,-2)$, and $\mathbf{C}_0[L_y = 5] = (5,-4)$ cylinders only in the 120° and the SL phase regions. We also consider a YC4 structure in the columnar and the SL phase regions [occasionally, the YC3 and $\mathbf{C}_0[L_y = 4] = (5,-4)$ systems are employed in the columnar phase region, however, they are frustrating some forms of the collinear ordering, see below]. For finite-length cylinders, we fix L_x to a value that after which, an increase of the cylinder's length would not change the average bond energy in the bulk of the system up to numerical uncertainties coming from the DMRG systematic errors [54,93]. In $L_x = \infty$ iDMRG calculations, we use YC6 and YC12 structures in all regions, reserving YC9 only for the 120° region, plus YC8 and YC10 in the columnar phase. We always set an efficient mapping for the infinite cylinders that minimizes the one-dimensional range of NN and NNN interactions, as shown in Fig. 1. Finally, to calculate bipartite quantities, such as reduced density matrix, $\tilde{\rho}$, and entropy of the DMRG wave functions [54], we make a cut that does not cross any Y direction bond and creates partitions L and R, as shown in the figure.

We now present an overview of how to calculate higher moments of an (possibly nonlocal) observable in a translation-invariant infinite-size system. This is required for the measurements of the cumulants and Binder ratios of the magnetization order parameters (see below). For symmetry broken (or symmetry protected) states, the Binder cumulant of the (string) order parameter can be evaluated directly in the thermodynamic limit [95]. However, in this case, because we preserve SU(2) symmetry, the magnetic order parameter is strictly zero and the Binder cumulant is not well defined. However, as we show below, the moments can still be used to detect the signature of magnetic ordering. Suppose we are interested in calculating the matrix elements of the moments of an order parameter MPO, $\mathbf{M}^{[k]}$, of dimension $\tilde{m}$, that transforms under SU(2) as a rank-k tensor. The explicit preservation of SU(2) symmetry leads to the vanishing of the order parameter, but the even moments can be nonzero. In this case, the measurement of the expectation values of the higher-order magnetic moments, $\langle M^n \rangle$ (of order n), is of interest. These can be done using the method of the *transfer operator* [92]. The generalized transfer (super-)operator, $\mathbb{T}_X$, associated with some operator of finite support (acting on a unit cell of an iMPS), $\hat{X}$, is defined as

$$\mathbb{T}_X(E^a) = \sum_{s's} \langle s'|\hat{X}|s\rangle A^{s'\dagger} E^a A^s, \tag{2}$$

where A^s are ordinary MPS matrices and E^a denote the so-called $\mathbf{E}$ matrices. In this context, E^a is essentially an eigenmatrix, however, the $\mathbf{E}$ matrices are more familiar for their role in the expectation value of an MPO $\langle \mathcal{A}|\hat{M}|\mathcal{A}\rangle$ (see Refs. [53,55] for full details). E^a is, in principle, extensive, and on an n-site system, can be defined recursively as

$$E^{a'}(n) \equiv \sum_{s',s,a} \mathcal{A}^{s'_n\dagger} M^{s's}_{a'a} \mathcal{A}^{s_n} E^a(n-1). \tag{3}$$

In the following example, for the sake of the simplicity we assume an one-site unit cell, although, in practice, for a magnetically ordered system the unit cell will be at least as large as the number of sublattices; the generalization for larger unit-cell sizes is straightforward. We give an example here for the second moment, the higher moments can be obtained recursively [92]. To calculate the asymptotic limit of $\langle M^2 \rangle$, one only needs to solve the diagrammatic fixed-point equation shown in Fig. 2(a), where the E^a matrices are connected according to

$$E^i(L+1) = \mathbb{T}_{M_{ii}}(E^i(L)) + \sum_{j>i} \mathbb{T}_{M_{ij}}(E^j(L)), \tag{4}$$

which can be solved sequentially, from E^1, E^2, ..., $E^{\tilde{m}}$. In practice, Fig. 2(a) shows the fixed point at which the addition of an extra site (or unit cell) to E^a matrices will leave the system unchanged. The MPO form of the order parameter on a unit cell can be written [53,55] as a supermatrix (a matrix where elements are local operators acting on a single site or unit cell of the lattice):

$$M = \begin{pmatrix} I & X \\ & I \end{pmatrix}, \tag{5}$$

and we can attach SU(2) quantum numbers $S = 0,1$ to the rows/columns. The operator for the second moment has the form

$$M^2 = \begin{pmatrix} I & X \\ & I \end{pmatrix} \otimes \begin{pmatrix} I & X \\ & I \end{pmatrix} = \begin{pmatrix} I & X & X & X^2 \\ & I & 0 & X \\ & & I & X \\ & & & I \end{pmatrix} \Rightarrow \begin{pmatrix} I & X & X^2 \\ & I & 2X \\ & & I \end{pmatrix}, \tag{6}$$

where in the last step, we have collapsed the middle rows to create a 3×3 matrix with new quantum numbers of $S = 0,1,0$ labeling the rows (assuming here that we want to calculate only the scalar part of X^2: for the calculation of higher moments we need the other spin projections too). We can now write the fixed point of the last MPO in the form of recursive equations for the E^a matrices, as shown in Figs. 2(b)–2(d). We note that the objects that appear on the right-hand sides of the figures are nothing other than the generalized transfer operators. Translating the graphical notation into equations, for example, Fig. 2(b) can be written as

$$E^1(L+1) = \mathbb{T}_I(E^1(L)), \tag{7}$$

which means $E^1(L)$ is an eigenmatrix of the transfer operator, which, for a properly orthogonalized MPS is just the identity matrix, so $E^1(L) = I$. As a result, equations for Fig. 2(c) and (d) can be written as

$$\begin{aligned} E^2(L+1) &= \mathbb{T}_X(I) + \mathbb{T}_I(E^1(L)) \\ &= C_X + \mathbb{T}_I(E^1(L)), \end{aligned} \tag{8}$$

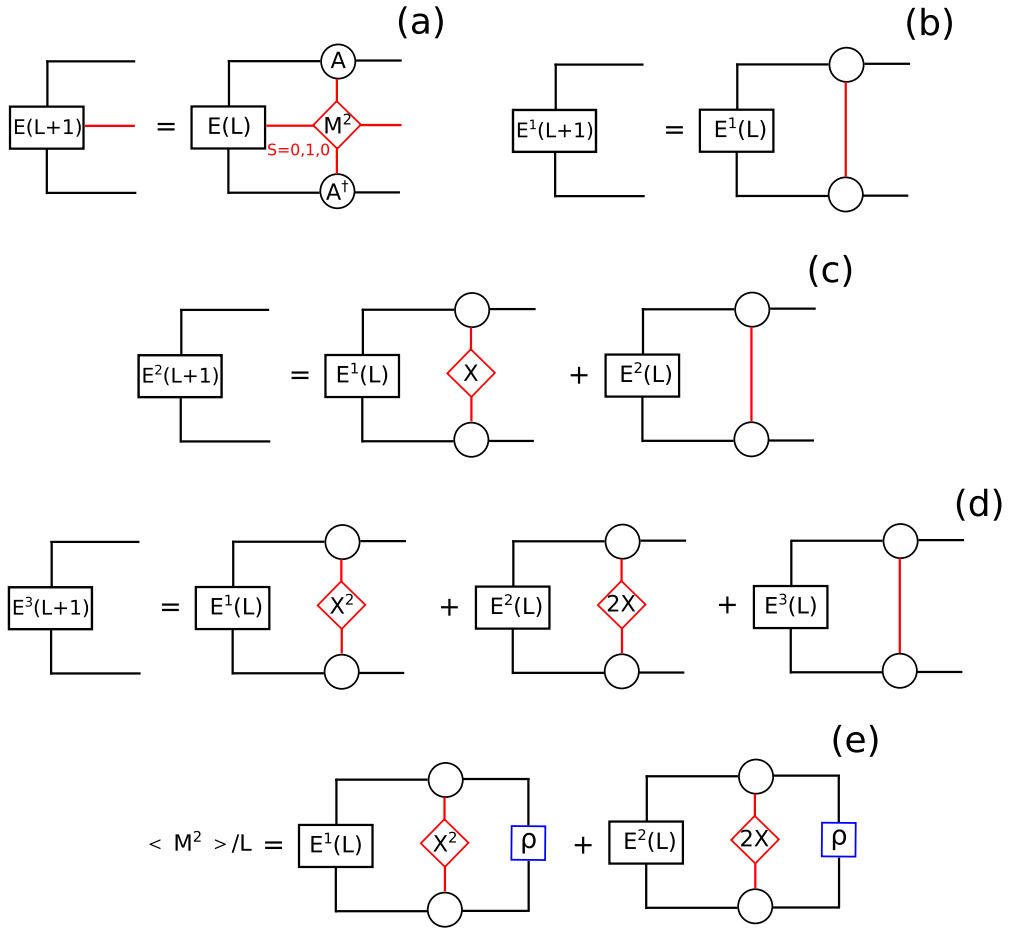

FIG. 2. (a) MPS diagram for the fixed-point equation of E^a matrices of the second moment of $\mathbf{M}$. MPS diagrams for the (b) first, $S = 0$, (c) second, S=1, and (d) third, $S = 0$, columns of $\mathbf{M}^2$, Eq. (6). (e) The MPS recipe to calculate the final expectation value of the second moment.

where $C_X = \mathbb{T}_X(I)$ is a constant matrix, and

$$E^3(L+1) = \mathbb{T}_{X^2}(I) + 2\mathbb{T}_X(E^2(L)) + \mathbb{T}_I(E^3(L)). \quad (9)$$

The desired expectation value is encoded in the final matrix, i.e., $\langle M^2 \rangle = \mathrm{Tr}(E^3\tilde{\rho})$. However, importantly, most of the matrix elements of E^3 do *not* contribute to the expectation value of the second moment per site, we need only the component of E^3 that has nonzero overlap with $\tilde{\rho}$. Note that $\tilde{\rho}$ is the right eigenmatrix of $\mathbb{T}_I$ with the unity eigenvalue, hence the component of E^3 that gives the expectation value is the component in the direction of the corresponding left eigenmatrix of $\mathbb{T}_I$.

The calculation of the matrix elements of E^2 can be done efficiently using a linear solver. To see how this works, consider the eigenmatrix expansion for the transfer operator, $\mathbb{T}_I = \sum_{n=1}^{m^2} \eta_n |\eta_n)(\eta_n|$, to obtain the eigenvalues η_n and eigenvectors $|\eta_n)$. If we write C_X and E^2 matrices in this $\{|\eta_n)\}$ basis with expansion coefficients $c_n^{(2)}$ and $e_n^{(2)}(L)$,

$$C_X = \sum_{n=1}^{m^2} c_n^{(2)} |\eta_n),$$

$$E^2(L) = \sum_{n=1}^{m^2} e_n^{(2)}(L) |\eta_n), \quad (10)$$

then Eq. (8) is, for each component,

$$e_n^{(2)}(L+1) = c_n^{(2)} + \eta_n e_n^{(2)}(L). \quad (11)$$

Following [92], we further decompose the coefficients into a component parallel and components perpendicular to the identity matrix, I (i.e., the left eigenmatrix of $\mathbb{T}_I$, which has the largest eigenvalue of $\eta_1 = 1$ due to the MPS orthogonalization condition), and define

$$\tilde{C}_X = \sum_{n=2}^{m^2} c_n^{(2)} |\eta_n),$$

$$\tilde{E}^2(L) = \sum_{n=2}^{m^2} e_n^{(2)}(L) |\eta_n), \quad (12)$$

so that $C_X = \tilde{C}_X + c_1^{(2)} I$ and $E^2 = \tilde{E}^2 + e_1^{(2)} I$. The reason for this is that the component in the direction of the identity $e_1^{(2)}$ diverges in the summation, whereas the other components that are perpendicular to the identity do not. Hence we need to find the fixed points of these parts separately.

Solving Eq. (11) for the parallel components reveals the local expectation value of X per site, which is a straightforward calculation:

$$e_1^{(2)}(L+1) = e_1^{(2)}(L) + c_1^{(2)}, \quad (13)$$

where $c_1^{(2)}$ is just the expectation value of the order parameter on one site. Hence $e_1^{(2)}(L+1) = \sum_{i=1}^{L}\langle X_i\rangle$, which is zero because of the SU(2) symmetry [indeed, $c_1^{(2)} = 0$ by construction, since it is in the wrong quantum number sector for the identity eigenvector of the transfer operator]. The perpendicular components lead to

$$\tilde{E}^2_{(n)}(L+1) = \tilde{C}_{(n)} + \eta_n \tilde{E}^2_{(n)}(L), \tag{14}$$

where now $n \geqslant 2$, and the eigenvalues $|\eta_n| < 1$. Thus Eq. (14) is of the form of the sum of a convergent geometric series. Upon taking the limit $L \to \infty$ and writing back the projection operators as the original matrices, Eq. (14) converges to a fixed point:

$$(1 - \mathbb{T}_I)\tilde{E}^2(\infty) = \tilde{C}_X, \tag{15}$$

which is a rather simple system of linear equations, and is numerically stable because the condition number of $1 - \mathbb{T}_I$ is simply related to the leading correlation length, $1/(1 - |\eta_2|) \simeq \xi$. In practice, the generalized minimal residual method (GMRES) is a good choice of linear solver for Eq. (15). Upon obtaining the matrix elements of $\tilde{E}^2$, we can proceed to calculate the final expectation value as shown in Fig. 2(e). Note that this does not require all of the matrix elements of E^3, since we only require the overlap between E^3 and the density matrix (the right eigenvector of $\mathbb{T}_I$ with eigenvalue 1). This means that $\langle M^2\rangle = L \times \mathrm{Tr}[\tilde{\rho}\mathbb{T}_{X^2}(I) + 2\tilde{\rho}\mathbb{T}_X(E^2(L))]$, which is demonstrated in the MPS diagrammatic equation of Fig. 2(e). That is, the only unknown is the E^2 matrix. This is a useful optimization and rather general—in calculating the expectation value of a triangular MPO of dimension $\tilde{m}$, only the matrix elements up to $E^{\tilde{m}-1}$ are required.

For calculating the fourth moment of a magnetization order parameter using SU(2) symmetry, X^4 decomposes as

$$X^4 = (\mathbf{X}\cdot\mathbf{X})^2 + (\mathbf{X}\otimes\mathbf{X})\cdot(\mathbf{X}\otimes\mathbf{X}), \tag{16}$$

where the dot product $\mathbf{X}\cdot\mathbf{X} = -\sqrt{3}[\mathbf{X}\times\mathbf{X}]^{[0]}$ and outer product $\mathbf{X}\otimes\mathbf{X} = \sqrt{6/5}[\mathbf{X}\times\mathbf{X}]^{[2]}$ are proportional to the $S = 0$ and $S = 2$ projections of the operator product, respectively, with an additional factor arising from the SU(2) coupling coefficients. In general, we would need to also include the cross-product term $(\mathbf{X}\times\mathbf{X})\cdot(\mathbf{X}\times\mathbf{X})$ (proportional to the spin-1 projection), however, this vanishes due to antisymmetry under time reversal.

III. OVERVIEW OF THE PHASE DIAGRAM

In this section, we present our findings for the phase boundaries and properties of Eq. (1), for different J_2/J_1 with $J_1 > 0$, using iDMRG and some benchmark comparisons using fDMRG. In Fig. 3, we show the summary of the phase diagram, with four distinct phases; two phases with symmetry-broken magnetic order, a Z_2 spin liquid, and (only for the $YC6$ geometry) an algebraic spin liquid. For each of these phases, we present below visualizations of the correlation functions, obtained from well-converged iDMRG ground states. In these visualizations, we depict spin-spin correlations, $\langle\mathbf{S}_i\cdot\mathbf{S}_0\rangle$, with respect to a reference site $\mathbf{S}_0$, using the size and the color of some spheres, and the NN correlators are depicted using the thickness and the color of some bonds. The reference site is denoted with the gray sphere. We also present the SSF up to the second Brillouin zone. Using the discrete Fourier transform of the real-space correlations to switch to momentum space, one can write

$$\mathrm{SSF}(\mathbf{k}, N=\infty) = \lim_{N\to\infty}\frac{1}{N}\sum_{i,i'}^{N}\langle\mathbf{S}_i\cdot\mathbf{S}_{i'}\rangle e^{i\mathbf{k}\cdot(\mathbf{r}_i-\mathbf{r}_{i'})}, \tag{17}$$

where $\mathbf{r}_i$ denotes the position vector of a spin $\mathbf{S}_i$ in the *planar* map of the lattice. The momentum vector $\mathbf{k}$ will sweep the extended Brillouin zones. When the momentum vector coincides with the lattice's wave vector $\mathbf{Q}$, the occurrence of the condition $\lim_{N\to\infty}\frac{\mathrm{SSF}(N)}{N} = \mathrm{Const.}$ guarantees the existence of true LRO. Plotting the SSF in the (k_x,k_y) plane will reveal the occurrence of strong FM correlations as Bragg peaks. However, for a fixed-L_y infinite cylinder, one can only estimate the sums appearing in Eq. (17) using a finite length correlation. Therefore we consider a large enough *cutoff* as an upper limit for i, namely N_c. We note that it is possible to obtain $SSF(\mathbf{k}, N=\infty)$ directly using the same method as described above for the moments (see also Ref. [92]), however, this is an expensive process and for calculating the entire $\mathbf{k}$ space it is much faster to calculate the real-space correlations and perform a Fourier transform. Here, we truncate the real-space correlation at the first point where $|\langle\mathbf{S}_0\cdot\mathbf{S}_{N_c}\rangle| \leqslant 10^{-5}$ is met for the nonmagnetic short-range correlated states (i.e., spin liquids) and the condition $|\langle\mathbf{S}_0\cdot\mathbf{S}_{N_c}\rangle| \leqslant 10^{-3}$ is met for the symmetry-broken quasi-LROs (i.e., 120° and columnar states). The obtained phases are the following.

(1) $J_2 \to -\infty$. In this limit, one can readily show that the lattice decouples into *three* sublattices, each of which is an NN triangular lattice with bond strength J_2. In the case of vanishing interactions between sublattices ($J_2/J_1 \to -\infty$), the ground state for each sublattice is trivially a fully saturated ferromagnet (see also Ref. [79]) with total spin magnetization of $S^{\mathrm{total}}_{A,B,C} = \frac{L_u}{2}$ per unit cell of each sublattice (A, B, or C). For a width-L_y infinite-length YC structure, $L_u = L_y/3$ and $S^{\mathrm{total}}_{A,B,C} = L_y/6$. The overall state can be any arbitrary mixture of three $\mathbf{S}^{\mathrm{total}}_A$, $\mathbf{S}^{\mathrm{total}}_B$, and $\mathbf{S}^{\mathrm{total}}_C$ spin vectors, where they only have to follow the angular momentum summation rules. This will cause a large degeneracy for the overall ground state, supporting total magnetization in a range of $0 \leqslant S^{\mathrm{total}} \leqslant \frac{3L_u}{2}$. Perturbing the Hamiltonian with a positive J_1 would then break this degeneracy and impose a 120°-ordered ground state.

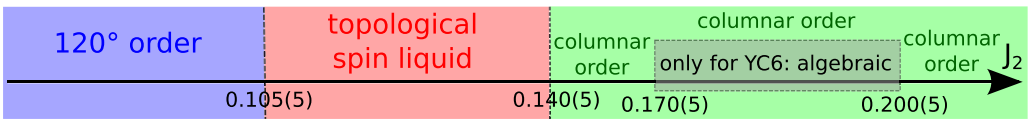

FIG. 3. Schematic phase diagram of the J_1-J_2 THM, Eq. (1), on infinite cylinders. Phase transition boundaries are obtained from the Binder ratios of the magnetization order parameter (see below).

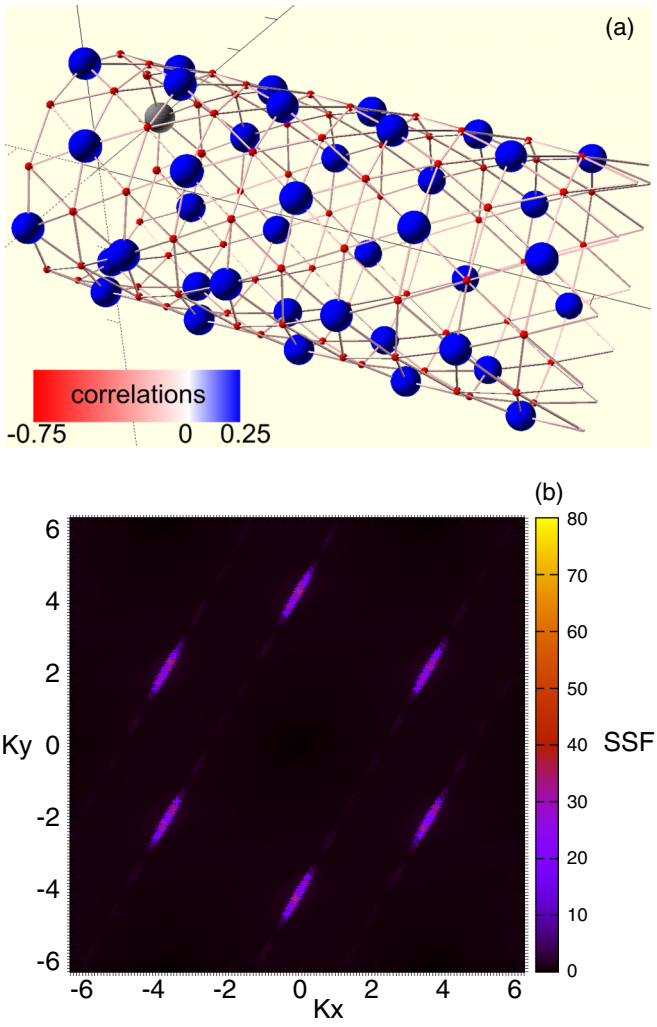

FIG. 4. Lattice visualizations for the iDMRG ground states of the THM on infinite cylinders at $J_2 = -1.0$ (120° order). (a) Correlation function for a YC12 system. The size and the color of the spheres indicate the (long-range) spin-spin correlations in respect to the principal (gray) site, and the thickness and the color of the bonds indicate the strength of the NN correlations. (b) SSF for a YC6 system. Bragg peaks are presented up to the second Brillouin zone of the inverse lattice.

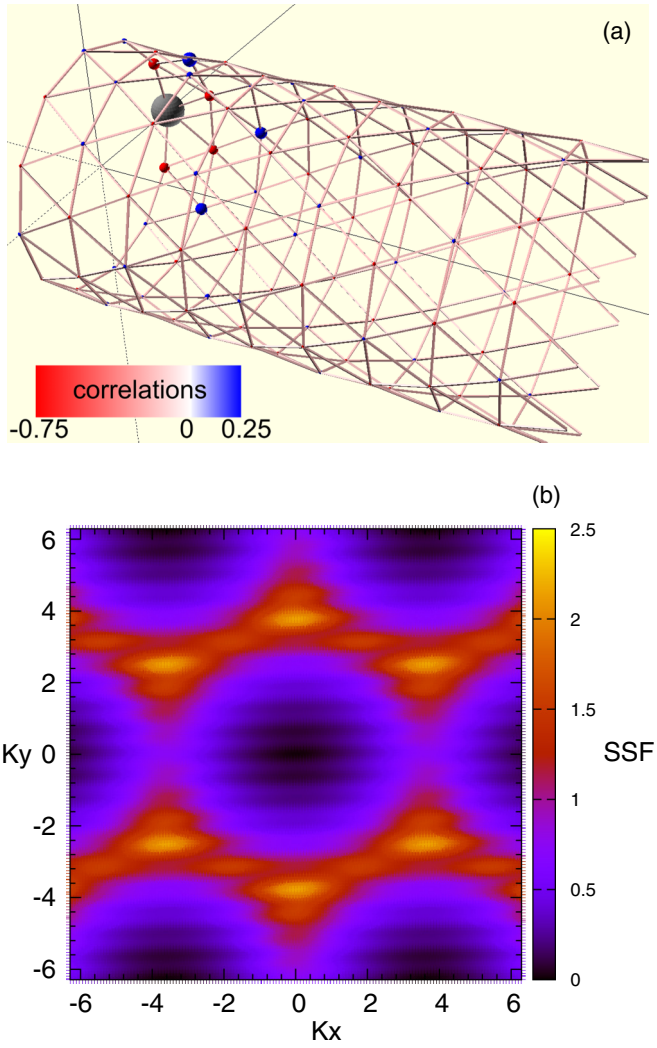

FIG. 5. Lattice visualizations for the iDMRG ground states of the THM on infinite cylinders at $J_2 = -0.125$ (topological spin liquid). (a) Correlation function for a YC12-$\hat{\imath}$ system. The size and the color of the spheres indicate the (long-range) spin-spin correlations in respect to the principal (gray) site, and the thickness and the color of the bonds indicate the strength of the NN correlations. (b) SSF for a YC10-$\hat{\mathrm{b}}$ system. Bragg peaks are presented up to the second Brillouin zone of the inverse lattice.

Similarly to the case of three-leg cylinders [79], we find no signs of a phase transition for any $J_2 < 0$.

(2) $J_2 \leqslant 0.105(5)$. The ground state is a coplanar quasiclassical 120° order. Our investigations on infinite YC6, YC9, and YC12 structures find a three-sublattice magnetic ordered state exhibiting SSB in the thermodynamic limit (cf. Secs. VII and VIII). By imposing SU(2) symmetry, the low-lying Nambu-Goldstone modes are evident and viewing the infinite cylinder as a 1D system it appears as a 1D quantum critical gapless state (cf. Sec. V). In Fig. 4(a), we present the correlation function for a YC12 ground state at $J_2 = -1.0$. The appearance of $\frac{L_y}{3} = 4$ blue (ferromagnet) spheres per ring exhibiting a roughly constant size (for short distances) and all-AFM (red) bonds (throughout the cylinder) are characteristics of the phase. In Fig. 4(b), we present the SSF for a YC6 ground state, deep in the 120° phase. The formation of *six* strong Bragg peaks on a slightly-distorted regular hexagon is another characteristic for the phase. Using this data, we predict a wave vector of $Q_{120^\circ} \approx (\pm 3.64, \pm 2.09)$, which is very close to our expected theoretical value of $Q^{\text{theory}}_{120^\circ} = (\pm\frac{2\pi}{\sqrt{3}}, \pm\frac{2\pi}{3}) \approx (\pm 3.63, \pm 2.09)$ for a 120° product state [4,70,71,79]. We note that the correlation functions of YC6 and YC9, and SSFs of YC9 and YC12 structures in the 120° phase are essentially identical to the results of Fig. 4.

(3) $0.105(5) \leqslant J_2 \leqslant 0.140(5)$. The ground state is a fourfold degenerate toric-code-type Z_2 topological spin liquid (denoted by YCL_y-$\hat{\mathrm{a}}$ for the anyonic sector $\hat{\mathrm{a}} \in \{\hat{\imath}, \hat{\mathrm{b}}, \hat{\mathrm{f}}, \hat{\mathrm{v}}\}$; see Ref. [85] for full details). In Fig. 5(a), we present the correlation function for a YC12-$\hat{\imath}$ ground state at $J_2 = 0.125$. The appearance of spheres with rapidly decaying radii and relatively weak all-AFM (red) bonds throughout the cylinder,

is characteristic of the SL states (such a behavior of the correlations is also observed for other topological sectors and system sizes, except there exist some weak bond anisotropies [77,85]). In Fig. 5(b), we present the SSF for a YC10-$\hat{b}$ ground state at $J_2 = 0.125$. The spectral function is almost homogeneous, although being noisy and containing some weak diffusive peaks (compared to the strong Bragg peaks of magnetically ordered states) reminiscent of gradual disappearance of the 120° order. We notice that this overall pattern is virtually the same for all anyonic sectors and system sizes. Furthermore, our qualitative studies demonstrate that the homogeneity of the SSF is growing with increasing L_y (not shown in the figures).

For the topological SL phase, we find the lower and upper phase boundaries of $J_2^{\text{low}} = 0.105(5)$ and $J_2^{\text{high}} = 0.140(5)$, respectively. Using fDMRG for rather small YC6 widths (see below) we obtain similar results, $0.101(4) \leqslant J_2 \leqslant 0.136(4)$. These phase boundaries are fairly close, but not identical, to those found by other authors [74–78,82–84].

(4) $0.140(5) \leqslant J_2 \leqslant 0.5$, but excluding a region *only for YC6* of $0.170(5) \leqslant J_2 \leqslant 0.200(5)$. The ground state is a quasiclassical collinear columnar (striped) order. Our investigations on infinite YC6, YC8, and YC10 structures (plus few more J_2 points on YC12 structures) show that that the columnar order is a two-sublattice AFM state exhibiting SSB in the thermodynamic limit (cf. Secs. VII and VIII). Again, with SU(2) symmetry, the state appears on an infinite cylinder as 1D quantum critical. The correlation function for a YC12 ground state at $J_2 = 0.5$ is presented in Fig. 6(a), where the appearance of robust FM stripes in the $\mathbf{a}_{+60^\circ}$ direction is clearly recognizable. In fact, the columnar order on the triangular lattice has three possible arrangements [96] of FM stripes, each aligning with one of the three principal lattice directions, which are only degenerate in the thermodynamic limit. For the THM on three-leg (trivially) and four-leg cylinders (both finite and infinite-length cases), we found that the columnar order always has FM stripes in the lattice short (Y) direction, while for wider-width finite-length YC structures, FM stripes will be in either of $\mathbf{a}_{+60^\circ}$ or $\mathbf{a}_{-60^\circ}$ directions, producing only *two* degenerate ground states.

We numerically confirmed that, upon choosing a suitable wave function unit cell, iDMRG states randomly converge to one of these two states. We present the SSF for a YC8 ground state at $J_2 = 0.5$ (with $\mathbf{a}_{+60^\circ}$ direction FM stripes), in Fig. 6(b). The formation of *four*, comparatively very strong Bragg peaks on a slightly-distorted regular parallelogram (with 60° angles) is a characteristic of the phase. A wave vector of $Q_{\text{striped}} \approx \pm(1.82,3.18)$ can be estimated for the SSF, which is close to our expected theoretical value of $Q_{\text{striped}}^{\text{theory}} = \pm(\frac{\pi}{\sqrt{3}},\pi) \approx \pm(1.81,3.14)$ for a columnar product state [70,71,79]. We note that the SSFs of the columnar orders on YC6, YC10, and Y12 systems are rather similar to this result, however, the wave vector changes to $Q_{\text{striped}}^{\text{theory}} = \pm(\pi,-\frac{\pi}{\sqrt{3}})$, when the direction of FM stripes are switched. Our numerical calculations extend only to $J_2 = 0.5$. However, we expect that there will be some additional geometry-dependent magnetically ordered phases for larger J_2 before reaching the large J_2 limit (see below).

(5) $0.170(5) \leqslant J_2 \leqslant 0.200(5)$, only for YC6. The YC6 geometry appears special in that we find signatures of an algebraic spin liquid, rather distinct from any other phase that we have observed in the model. Our results suggest that this phase is a quantum critical, gapless state with power-law scaling of the correlation function (cf. Sec. V) and *no* magnetic order. In Fig. 7, the presented correlation function and SSF appear to be reminiscent of a columnarlike ordering, but there are subtle differences. The size of spheres, representing the two-point correlation function, Fig. 7(a), decays faster than the columnar phase. In addition, the sizes of SSF peaks, Fig. 7(b), are considerably smaller than the typical size of the Bragg peaks in the columnar order having the same system width. In Secs. VII and VIII, below, we show that this phase has no signatures of magnetic ordering, which indicates that there are no broken symmetries and hence some kind of algebraic spin liquid.

(6) $J_2 \to +\infty$. Following the arguments presented for the $J_2 \to -\infty$ case, in the limit of $|J_2| \gg 1$, the physical

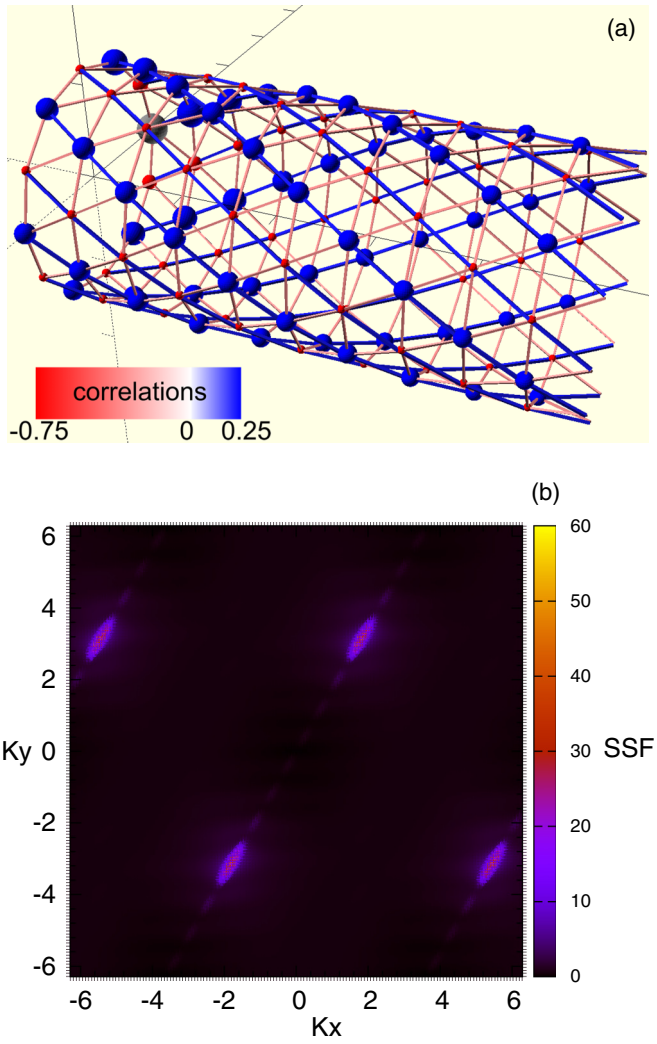

FIG. 6. Lattice visualizations for the iDMRG ground states of the THM on infinite cylinders at $J_2 = 0.5$ (columnar order). (a) Correlation function for a YC12 system. The size and the color of the spheres indicate the (long-range) spin-spin correlations in respect to the principal (gray) site, and the thickness and the color of the bonds indicate the strength of the NN correlations. (b) SSF for a YC8 system. Bragg peaks are presented up to the second Brillouin zone of the inverse lattice.

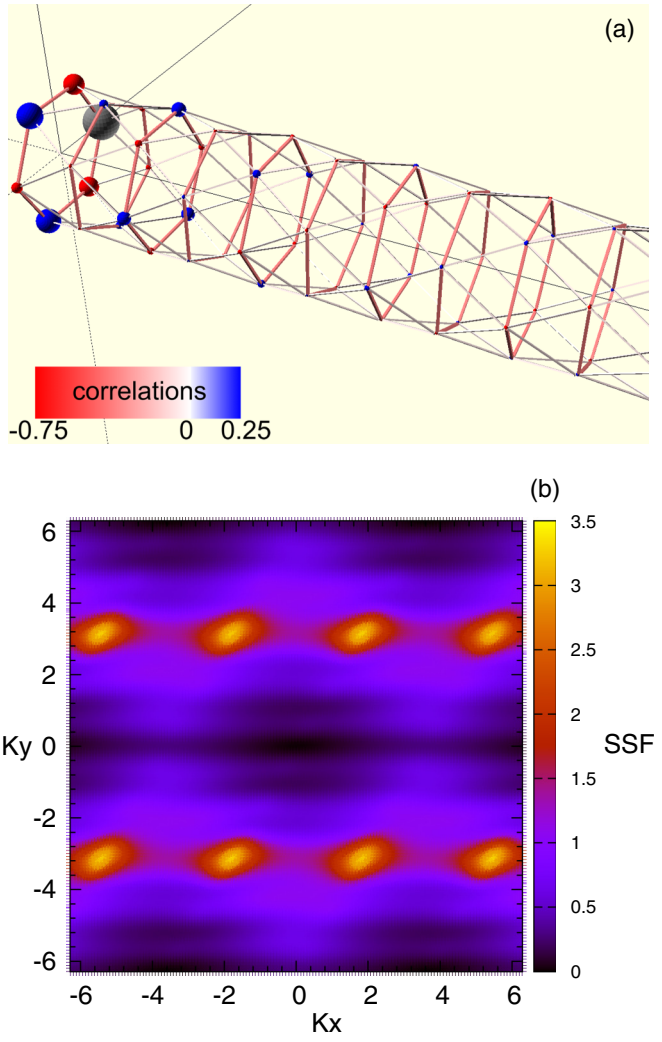

FIG. 7. Lattice visualizations for the iDMRG ground state of the THM on an infinite YC6 system at $J_2 = 0.185$ (ASL phase). (a) Correlation function results, where the size and the color of the spheres indicate the (long-range) spin-spin correlations in respect to the principal (gray) site, and the thickness and the color of the bonds indicate the strength of the NN correlations. (b) SSF results, where the Bragg peaks are presented up to the second Brillouin zone of the inverse lattice.

lattice will transform to three decoupled sublattices with antiferromagnetic NN bonds of the strength J_2. For $J_2 \to +\infty$, the ground state on each new sublattice is the same as the overall ground state for $J_2 = 0$, i.e., the 120° order. However, for few-leg ladder systems, other symmetry broken phases could appear due to the restricted geometry.

As an example, for three-leg finite cylinders [79] in $J_2 \to \infty$, we found that the ground state is three weakly coupled copies of a NNN Majumdar-Ghosh state. Interestingly, we found a similar dual Majumdar-Ghosh phase for four-leg finite cylinders [93]). Consistent with the expected 2D limit, we did not observe any signature of such Majumdar-Ghosh-type phases for $L_y > 4$ ladders. In addition, a semiclassical SWT study [70] confirms that the "order from disorder" mechanism would choose three-fold degenerate and decoupled states for $J_2 \gg 1$, which are energetically favorable to arrange according

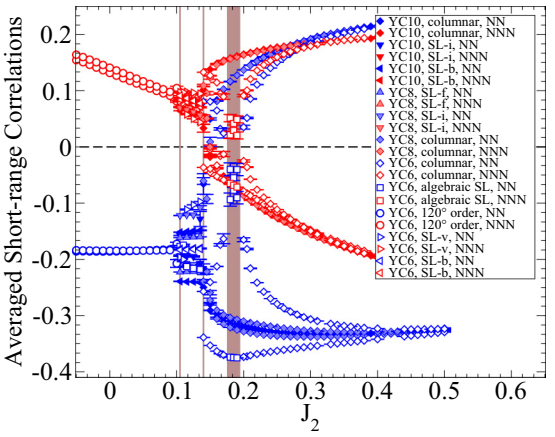

FIG. 8. Short-range correlation functions for the iDMRG ground states of the THM on YC6, YC8, and YC10 structures vs NNN coupling strength, J_2. Each correlator value is averaged over a wave-function unit cell, then extrapolated *linearly* with iDMRG truncation errors toward the thermodynamic limit of $m \to \infty$. For each J_2, red symbols represent NN bonds in principal Y, $\mathbf{a}_{+60^\circ}$, and $\mathbf{a}_{-60^\circ}$ directions. Similarly, blue symbols represent NNN bonds in nonprincipal directions of $\frac{1}{\sqrt{2}}(1,1)$, $\frac{1}{\sqrt{5}}(2,-1)$, and $\frac{1}{\sqrt{5}}(2,1)$. Narrow brown stripes indicate predicted phase transitions from the Binder ratio results. Thick brown stripe shows a speculated region for the existence of the ASL phase on YC6 structures (see below).

to 120° ordering. Hence we expect that such exotic ordered phases are particular features of narrow cylinders.

To get a better quantitative insight on the phase diagram of the THM, we study the short-range (NN and NNN) spin-spin correlations, $\langle \mathbf{S}_i \cdot \mathbf{S}_j \rangle$, Fig. 8. Short-distance correlators in a crystalline phase have a repetitive pattern reflecting the bulk properties of the ground state. In Fig. 8, we choose six reference bonds, including three NN and three NNN correlators, to build up a picture of the real-space correlations for different system widths. In the 120° phase region, correlators are very nearly isotropic, where NN (NNN) bonds are all AFM (FM). On the other hand, topological spin liquids on finite-width systems contain strong anisotropies [76,77], which is clearly seen in Fig. 8. As we showed previously [85], in the thermodynamic limit, anyonic sectors $\hat{\mathrm{b}}$ and $\hat{\mathrm{f}}$ are anisotropic on finite cylinders, while $\hat{\mathrm{i}}$ and $\hat{\mathrm{v}}$ are isotropic [97,98]. The behavior of the correlation functions is distinct in the columnar phase, where there are always *two* FM bonds (one is a NN and another one a NNN correlator) and *four* AFM bonds (two are NN and other two NNN correlators) out of the six reference bonds. The FM stripes of the columnar order can, of course, choose either one of $\mathbf{a}_{+60^\circ}$ or $\mathbf{a}_{-60^\circ}$ directions, so such data points in this region are exchangeable. Furthermore, curiously for YC6, in the ASL phase region $[0.170(5) \leqslant J_2 \leqslant 0.200(5)]$, the system temporarily restores all symmetries, again, by crossing the $\mathbf{a}_{\pm 60^\circ}$-direction bonds.

IV. DIRECT MEASUREMENT OF THE ORDER PARAMETERS ON FINITE-LENGTH CYLINDERS

To provide a verification of the phase boundaries for comparison against our iDMRG results, we calculated two magnetization order parameters on $L_y \leqslant 6$ finite-length

cylinders (small compare to the largest width of our infinite-length YC systems) using an approach originally suggested by White and Chernyshev [73]. Consider the arbitrary magnetization vector order parameter of $\mathbf{M}(m)$ for a wave function with m number of states [the preservation of the SU(2)-symmetry causes the structural vanishing of all projection components]. Upon a suitable choice of the system size and careful extrapolation toward the thermodynamic limit, nonzero values for the *second* moment of $\mathbf{M}$ (which is directly proportional to the spin susceptibility) can be derived. In White and Chernyshev's method, one first extrapolates the order parameter *linearly* with the DMRG truncation errors, ε_m, toward the thermodynamic limit of $m \to \infty$ ($\varepsilon_m \to 0$) to calculate $\langle \mathbf{M}^2(\infty) \rangle$. Then, using only fixed aspect-ratio ($\frac{L_y}{L_x} =$ Const.) system sizes, L_x and L_y should be simultaneously extrapolated toward the thermodynamic limit of $L \to \infty$. By employing a similar approach, plus some simple dimensional analyses and numerical examination of the magnetic moments, we suggest that in the MPS constructions of the SU(2)$S = 0$-sector ground states on fixed aspect-ratio cylinders ($L_x > L_y$), the normalized order parameter per site, $\mathbf{M}^2(\infty)$, scales as

$$\langle \bar{\mathbf{M}}^2(\infty) \rangle = \bar{a}_0 + \bar{a}_1 L_x^{-2} + \ldots, \tag{18}$$

where eclipses represent higher order terms in $\frac{1}{L_x}$ (note that Eq. (18) is only a heuristic fit; see Ref. [99] for theoretical predictions). One should note that any *independent* growth of L_x and L_y toward the $L \to \infty$ limit can be interpreted as the existence of an infinitely long cylinder at some stage. This will collapse the system, essentially, to an inherently 1D state, for which the behavior of the magnetic moments is essentially different (see below).

The magnetic order parameters that we selected to study the phase diagram on finite-size cylinders include the FM sublattice magnetization, defined arbitrarily on sublattice A,

$$O_A^{\mathrm{FM}} = \frac{2}{\sqrt{N_A(N_A+2)}} \sqrt{\langle \mathbf{S}_A^2 \rangle}, \tag{19}$$

where $\mathbf{S}_A = \sum_{i \in A} \mathbf{S}_i$ is summed over all sites in sublattice A, and $2/\sqrt{N_A(N_A+2)}$ is a normalization factor (N_A is the total number of sublattice-A spins on the finite lattice). O_A^{FM} is a well-defined order parameter for the 120° phase. The *classical* 120° order will result in the maximum possible value for the order parameter in the limit of $L \to \infty$, i.e., $O_A^{\mathrm{FM}}[\mathrm{classical}, L \to \infty] = 1$ [93]. The next order parameter is the staggered magnetization, $\mathbf{M}_{\mathrm{stag}}$, for which the second moment is a well-defined order parameter for the columnar phase,

$$O^{\mathrm{stag}} = \frac{1}{L} \sqrt{\langle \mathbf{S}_{\mathrm{stag}}^2 \rangle}, \tag{20}$$

where $\mathbf{S}_{\mathrm{stag}} = \mathbf{S}_A - \mathbf{S}_B$ is the staggered magnetization for sublattices A and B. The *classical* columnar order will result in the maximum possible value for the order parameter in the limit of $L \to \infty$, i.e., $O_{\mathrm{stag}}[\mathrm{classical}, L \to \infty] = 1$ [93].

Our results for O^{FM} and O^{stag}, in the thermodynamic limit of $L \to \infty$, are presented in Fig. 9. Individual error bars are relatively large, but the overall behavior of the magnetization curves follows the expected pattern: there exists a small region for J_2, where both $O^{\mathrm{FM}}(L \to \infty)$ and $O^{\mathrm{stag}}(L \to \infty)$ are touching the zero axis (considering uncertainties), which

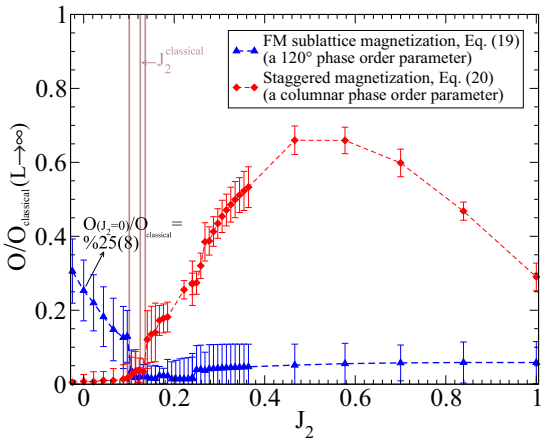

FIG. 9. fDMRG results for the magnetization order parameters of the THM, O_A^{FM}, Eq. (19), and O^{stag}, Eq. (20), in the thermodynamic limit of $L \to \infty$. Each data point represents a separate extrapolation (and the resulting error) with the method of the fixed-aspect-ratio, Eq. (18). A variety of cylindrical structures have been used for extrapolation purposes, as listed in Sec. II. Brown (outer) stripes are predicted phase boundaries, while the middle stripe is the classical phase transition at $J_2 = 0.125$ [69].

provides SL region boundaries, $J_2^{\mathrm{low}} = 0.101(4)$ and $J_2^{\mathrm{high}} = 0.136(4)$. Next to the SL phase region, on the left, only $O^{\mathrm{stag}}(L \to \infty)$ is touching the zero axis, while $O^{\mathrm{FM}}(L \to \infty)$ are increasing for $J_2 \to -\infty$ (confirming the stabilization of 120° order in this region). On the other hand, next to the SL phase region on the right, $O^{\mathrm{stag}}(L \to \infty)$ increases rapidly, indicating columnar order. Interestingly, the value of $O^{\mathrm{FM}}(L \to \infty)$ ($O^{\mathrm{stag}}(L \to \infty)$) is increasing (decreasing) again for large J_2. This is consistent with the existence of a multi-component 120° order (three copies of a conventional 120° order placed on sublattices; see Sec. III) in the $J_2 \to \infty$ limit.

It is worth noting the magnitude of the sublattice magnetization at $J_2 = 0$ (NN model). The measurement of variants of a 120°-order parameter for the NN model has been in the center of attention [69,72,74,75,79] to understand the degree of magnetization reduction (in comparison to their classical counterparts) in such a frustrated model. As shown in Fig. 9, we predict $O^{\mathrm{FM}}[J_2 = 0]/O^{\mathrm{FM}}[\mathrm{classical}] = 25(8)\%$, which is considerably smaller than approximate results of 50% by SWT [69], 48% by ED [72], 40% by CCM [75], and 50% by variational QMC [74].

V. CORRELATION LENGTHS

For infinite cylinders, the gapped or gapless nature of the ground state can be understood through the study of the (principal) correlation length ξ, since the behavior of the magnetic ordering and the scaling behavior of the static correlation functions are connected (cf. Sec. I). Indeed, the Hastings-Oshikawa-Lieb-Schultz-Mattis theorem [100,101] relates the size of the energy gap Δ_e to ξ for local, translation-invariant Hamiltonians on even-width cylinders as $\xi \leqslant \frac{\mathrm{Const.}}{\Delta_e}$ (i.e., ξ^{-1} serves as an upper boundary for the gap size). For the (inherently one-dimensional) MPS *Ansatz*, the connection between entanglement scaling and the correlation length is

well understood [55,58,59]. In a critical phase, the correlation length diverges with a signature *power-law* scaling with the number of states as $\xi(m) = \tilde{\kappa}_c m^{\tilde{\kappa}}$. Furthermore, in such states, the entanglement entropy diverges with a scaling of $S_{EE} \sim \ln \xi$. On the other hand, for short-range gapped states, ξ saturates to a finite value as m is increased, which in the topological spin-liquid state of the THM is short; of the order of a few lattice spacings. Interestingly, as we see below, the correlation length scaling for magnetic ordering in SU(2)-symmetric MPS on infinite cylinders appears rather differently than the full 2D limit. Such cylindrical magnets exhibit some signatures of true LRO (e.g., in the ES, see below), however, due to the explicit preservation of SU(2) and the dominating 1D physics of the MPS *Ansatz*, the ground states emerge as quasi-LRO critical states (note that the correlation length can still diverge with respect to the cylinder circumference). Nevertheless, in the iMPS representation of the wave function, the correlation lengths (per unit cell) can be conveniently read from the eigenspectrum of the transfer operator, $\mathbb{T}_I$ (cf. Sec. II):

$$\frac{\xi_i(m)}{L_u} = -\frac{1}{\ln|\eta_i(m)|}, \quad i = 2,3,4,\ldots, \tag{21}$$

where η_i are eigenvalues of $\mathbb{T}_I$ (arranged as $\{|\eta_1| > |\eta_2| > |\eta_3| > \ldots\}$). η_i depends on the number of states, and are also labeled by an SU(2) spin sector, which is the symmetry sector of the (block diagonal) transfer operator, and corresponds to the symmetry of the associated correlation function. We have discarded $i = 1$, as the largest eigenvalue of $\mathbb{T}_I$ in an orthonormalized basis always corresponds to $\eta_1 = 1$ (belonging to the identity eigenmatrix) and the principal correlation length is the second largest eigenvalue, $\xi_{2,S} \equiv \xi_S$. For a phase with magnetic ordering, such as 120° and columnar order, the principal correlation length is expected to belong to the $S = 1$ sector, indicating that the slowest decaying correlations are in the spin-spin form. For the topological and algebraic spin liquid phases, we find that the principal correlation length is in the $S = 0$ sector, indicating that the slowest decaying correlation is some kind of singlet-singlet correlator (we have not determined the exact form). An undesirable effect of the variational convergence of the ground state using the iDMRG approach emerges from the constraint of SU(2) symmetry, whereby spurious symmetry effects make the wave function noninjective (the spectrum of $\mathbb{T}_I$ contains multiple identity eigenvalues in each S sector). We have removed such wave functions everywhere except in the immediate vicinity of the $J_2 = 0.105(5)$ transition (expectation values are still reliable), where the noninjectivity was difficult to avoid (this is likely due to the closeness of this point to the topological SL region).

We present the correlation length results for the ordered phases in Fig. 10, where we compared them against the ξ_S from the topological spin liquid [85]. We immediately notice that the principal correlation length belongs to the $S = 1$ sector for the magnetic ground states with 120° and columnar ordering, however, it switches to the $S = 0$ sector for all SL states, whether they are quasi-LROs (as in ASLs) or short-range correlated (as in topological spin liquids). We can see that both the ASL and the magnetically ordered states have *power-law* behavior, reflecting their gapless and quantum critical natures. We emphasize that in the case of the ASL, this behavior appears to be intrinsic; however, for the magnetically ordered phases, the power-law correlations are a consequence of preserving SU(2) symmetry. In contrast, for the topological spin liquid, the correlation length is considerably smaller in size (order of few lattice spacings) and qualitatively begins to saturate in the large-m limit, although it is surprisingly difficult to do a rigorous fit.

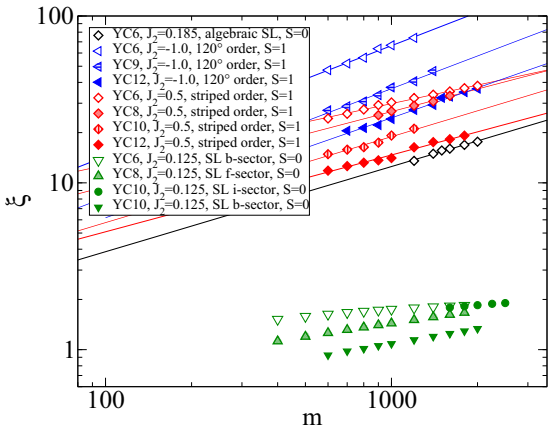

FIG. 10. iDMRG results for the principal correlation lengths (per unit-cell size) vs the number of states m in a variety of the detected phases and system sizes of the THM on infinite cylinders. Results are labeled with SU(2) quantum numbers, S. Lines are attempted power-law fits, $\xi = \tilde{\kappa}_c m^{\tilde{\kappa}}$, to quasi-LROs ensuring the existence of a critical phase (see also Sec. I). Green-symbol data are selected from Ref. [93] to provide comparison between the magnitudes and asymptotic behaviors of $\xi_S(m)$ in gapped and gapless phases.

VI. ENTANGLEMENT ENTROPY OF QUASI-LRO MAGNETS

The entanglement entropy is a central quantity in the physics of the many-body systems, which provides a measure of how strongly conjunct subsystems are entangled. The entropy has proven to be a powerful numerical tool for characterizing the low-energy spectrum, detection of SSB, and topological degeneracy of the ground state (for some examples, see Refs. [60,102–106]). Between many different approaches to measure entropy, we employ the method of Jiang *et al.* [107] that calculates the von Neumann entropy along a bipartition cut of the cylinder, as shown in Fig. 1, since it is computationally convenient to manipulate in the context of MPS and DMRG algorithms. The bipartite von Neumann entropy is defined as $S_{\rm EE} = -{\rm Tr}(\tilde{\rho}\ln\tilde{\rho})$. In terms of the eigenvalues of $\tilde{\rho}$, i.e., $\{\lambda_i\}$, the entropy can be written as $S_{\rm EE} = -\sum_i \lambda_i \ln\lambda_i$. Roughly speaking, $S_{\rm EE}$ counts the number of entangled pairs on the bipartite boundary. $S_{\rm EE}$ is a function of the $(D-1)$-dimensional *area* of the D-dimensional quantum system, i.e., the boundary size, $L_{\rm cut}$ (note that $L_{\rm cut} = L_y$ for the YC structure). In fact, robust theoretical studies [102,103,108,109] proved that for interacting 2D spin systems with only local couplings and a cut size significantly larger than the correlation length, the leading term in the entropy scales with the boundary area, $S_{\rm EE} \propto L_{\rm cut}$, not the system volume, which is known as the *area law* (the area law was originally introduced in the context of the black holes [110] and quantum field theory [111,112]). However, for strictly 1D quantum critical states (in the thermodynamic limit)

the condition of the boundary size being considerably larger than the correlation length *cannot* be met, and the $S_{\rm EE}$ behavior is modified. In this case, the leading term in the entropy relates to the only length scale of the system, i.e., the correlation length, as $S_{\rm EE} \sim \ln(L_{\rm eff}) \sim \ln(\xi)$ [58,59], where $L_{\rm eff}$ stands for the effective size of the system. For the symmetry-broken true LROs, again, the size of the cut is significantly smaller than the diverging correlation length and a logarithmic term should be added to the area-law behavior [106]:

$$S_{\rm EE} = \beta_0 + \beta_1 L_{\rm cut} + \frac{N_G}{2}\ln(L), \tag{22}$$

where β_0 corresponds to a nonuniversal constant, which depends on the system geometry, the topological entanglement entropy [102,103], spin stiffness, and the number, N_G, and the velocity of the Nambu-Goldstone excitations. In addition, β_1 is another nonuniversal constant, which depends on the short-range entanglement in the vicinity of the cut and a short-distance characteristic cutoff. For the (quasi-)LRO, SU(2)-symmetric, iMPS ground states on the infinite cylinders, we find that the entropy scaling behavior is distinct. As discussed in Sec. V, MPS-*Ansatz* symmetry broken magnets appear as quantum critical states on the cylinder. Thus it is expected that the entropy exhibits a *combination* of the area-law and the critical behaviors. Our numerical measurements on an SU(2)-symmetric, quasi-LRO ground state of the J_1-J_2 THM on the infinite YC structures confirms such a mixed scaling as of

$$S_{\rm EE} \simeq a_0(L_y) + a_1(L_y)\ln(\xi), \tag{23}$$

where

$$a_1(L_y) = \alpha_0 + \alpha_1 L_y. \tag{24}$$

The behavior of the nonuniversal constant of a_0 proved to be more challenging to predict, but it can only contain subleading corrections to the area-law term appearing in a_1 (see below).

In Fig. 11, we present our entropy measurements for the ground states of the THM deep in the *columnar* phase region. Due to exponential cost of the calculations with the system width we only obtained a few wave functions for different L_y in the columnar phase. However, the results shown in Fig. 11 confirm the prediction of Eqs. (23) and (24). In the figure, we first fit a line to the original entropy data and calculate a_0 and a_1 for each system size. Clearly, a_1 values are consistent with the area-law behavior. We measured the coefficients of a_1 as $\alpha_0 = -0.28(1)$ and $\alpha_1 = 0.068(1)$. In contrast, there was no obvious fit possible for a_0 values, but their saturating nature for the large-L_y limit is consistent with this term being a subleading correction to the mixed term containing the area-law behavior.

VII. NUMERICAL TOOLS I: CUMULANTS AND BINDER RATIOS OF THE MAGNETIZATION ORDER PARAMETERS

In Sec. II, we constructed the theoretical framework for a method to measure the nonlocal moments and cumulants of the magnetic order parameters, in the context of SU(2)-symmetric translation-invariant MPS, where all projection components of the magnetic order parameter $\mathbf{M}^{[k]}$ vanish by construction. In this case, the higher moments can play the role of the order parameter. It is convenient to connect the moments of the

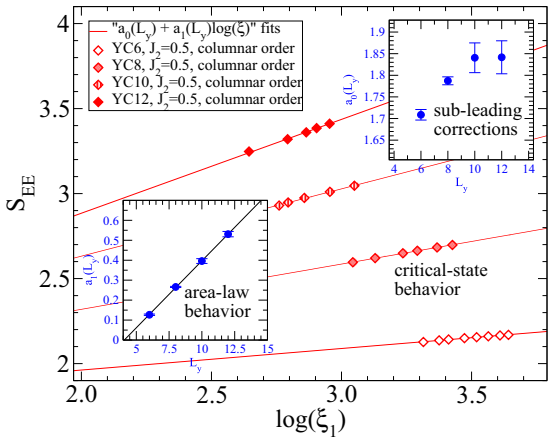

FIG. 11. iDMRG results for the entanglement entropy of the columnar order of the THM at $J_2 = 0.5$ on infinite-size YC systems with different system widths. In the main figure, entropies are plotted vs $S = 1$ correlation lengths ξ_1, and red lines are attempted fits according to Eq. (23), which is the predicted behavior for the quasi-long-range critical states on infinite cylinders. The scaling behaviors of a_0 and a_1 of Eq. (23) vs the system width are presented in the insets.

operators to the ith cumulant *per site*, κ_i, by employing

$$\langle M^n\rangle = \sum_{i=1}^{n} B_{n,i}(\kappa_1 L, \kappa_2 L, \ldots, \kappa_{n-i+1} L), \tag{25}$$

where $B_{n,i}$ are *partial Bell polynomials* [61] and L now stands for the operator length. For some examples, we expand Eq. (25) to write the relations for the first few cumulants:

$$\begin{aligned}
\langle M\rangle &= \kappa_1 L,\\
\langle M^2\rangle &= \kappa_2 L + \kappa_1^2 L^2,\\
\langle M^3\rangle &= \kappa_3 L + 3\kappa_2\kappa_1 L^2 + \kappa_1^3 L^3,\\
\langle M^4\rangle &= \kappa_4 L + \left(4\kappa_3\kappa_1 + 3\kappa_2^2\right)L^2 + 6\kappa_2\kappa_1^2 L^3 + \kappa_1^4 L^4.
\end{aligned} \tag{26}$$

The cumulants per site are obtained directly as the asymptotic large L limit obtained from the summation of the tensor diagrams presented in Sec. II. For the iMPS *Ansatz*, when the asymptotic limit is taken to derive a translation-invariant infinite-size system, one should replace the operator length with the effective system size as $L \to L_{\rm eff} \propto \xi$ (see also Sec. VI). Below, we introduced the magnetic order parameters that are used to measure the cumulants and characterize the LROs of the THM. We first construct the MPO forms of the higher moments of a *staggered magnetization* (the order parameter for columnar order on cylinders with FM stripes in $\mathbf{a}_{+60^\circ}$ direction),

$$\mathbf{M}_{\rm stag} = \sum_{i=1}^{L_y}(-1)^i \mathbf{S}_i, \tag{27}$$

and a *tripartite magnetization* (the order parameter for the 120° phase),

$$\mathbf{M}_{\rm tri} = \sum_{i\epsilon\langle A,B,C\rangle}^{L_y}\left(\mathbf{S}_{A_i} + e^{i\frac{4\pi}{3}}\mathbf{S}_{B_i} + e^{-i\frac{4\pi}{3}}\mathbf{S}_{C_i}\right), \tag{28}$$

on a L_y-size unit cell. Numerical computation of the moments of such order parameters is a challenging task due to relatively large dimensions of the resulting MPOs. Nevertheless, we succeeded to calculate the second cumulant, κ_2, and the fourth cumulants, κ_4, of M_{stag} and M_{tri} [the odd moments vanish due to the SU(2) symmetry] for a range of the ground states. We suggest that the most useful choice of cumulants is κ_4, which is connected to the *excess kurtosis* [61], γ_4, of the block distribution function associated with the operator $\mathbf{M}^{[k]}$:

$$\gamma_4 = \frac{\kappa_4}{\kappa_2^2 L}. \tag{29}$$

We emphasize that the above equation is only valid for the $\kappa_1 = \kappa_3 = 0$ case. The importance of the fourth cumulant was revealed by some studies on the fourth magnetic moment behavior of 2D Ising antiferromagnets [113,114], which established κ_4 as an effective tool for pinpointing quantum critical points. In these studies, the scaling behavior of the fourth magnetic moment is observed to vary significantly at an Ising transition (more precisely, κ_4 changes sign at the critical point, and changes by many orders of magnitude nearby the critical point). Another relevant and interesting (dimensionless) quantity is the Binder cumulant [50,115–117], $U_L = \frac{n_H+2}{2}(1 - \frac{n_H}{n_H+2}\frac{\langle \mathbf{M}^4\rangle}{\langle \mathbf{M}^2\rangle^2})$, where n_H is the number of projection spin operators used to construct the order parameter (e.g., $n_H = 3$ for a vector magnetization). In the vicinity of a critical point, the Binder cumulant becomes independent of the system size (lower moments of the order parameter cancel out higher-order finite-size effects) and can be used to pinpoint the transition. Previously, we adopted [79] U_L of a (scalar) dimer order parameter to locate a critical point in the phase diagram of the THM on three-leg cylinders. However, until now, the scaling behavior of U_L was less-known for the cases where the order parameter itself is strictly zero. In the limit of $L \to \infty$, as it is clear from Eq. (26), the higher-order corrections in $\langle M^n\rangle$ vanish and the conventional method of Binder cumulants for locating the phase transitions becomes ineffective. However, the correlation length ξ gives us a natural length scale and a rather precise process to scale a Binder-cumulant-type quantity in the vicinity of a critical point. As in the case of the entropy, Sec. VI, the key to obtaining the correct scaling of the magnetic moments of iMPS wave functions is to choose $L_{\text{eff}} = \tilde{s}\xi$, where $\tilde{s}$ is any *fixed* scaling constant. For Binder cumulant, $\tilde{s}$ has no qualitative effect except to change the value of the critical binder cumulant, similar to the role of boundary conditions for the finite-size Binder cumulant. Therefore one can freely choose $\tilde{s}$ to obtain the most numerically stable fit. When the order parameter is zero by symmetry, so that $\kappa_1 = \kappa_2 = 0$, the appearance of such a constant is irrelevant and only the ratio of the second and fourth cumulants plays a role. By replacing the explicit relations for $\langle \mathbf{M}^2\rangle$ and $\langle \mathbf{M}^4\rangle$ from Eq. (25) into U_L, we propose the ratio [which we call the "Binder ratio": see also Eq. (29)]:

$$U_r = \frac{\kappa_4}{\kappa_2^2 \xi}. \tag{30}$$

We find that numerically this combination of the moments and the correlation length removes much of the numerical noise that appears in the individual moments.

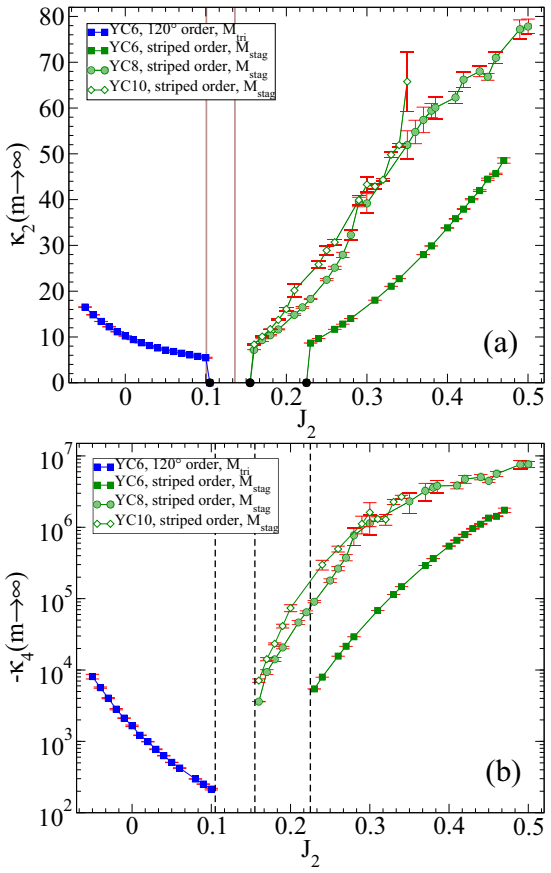

FIG. 12. iDMRG results for the extrapolated (a) second cumulants and (b) fourth cumulants of the magnetization order parameters, Eqs. (27) and (28), at the thermodynamic limit of $m \to \infty$, on a variety of phase regions and system widths of the THM. Each colored data-point represents a $\kappa_2(m \to \infty)$ value [$-\kappa_4(m \to \infty)$ value], which is the result of an extrapolation according to a power-law fit $\kappa = \breve{a}_0 + \breve{a}_1 e^{-\breve{a}_2 m}$ for $m \to \infty$ (see Ref. [93] for some examples on the individual extrapolations). In part (a), brown stripes are fDMRG results for the phase transition obtained from direct measurements of the local magnetization, Sec. IV. Solid circles, in part (a), and dashed-lines, in part (b), mark the borders beyond which an extrapolation was not possible due to the magnetic disorder.

We present the extrapolated results of κ_2 and $|\kappa_4|$ for $\mathbf{M}_{\text{stag}}$ and $\mathbf{M}_{\text{tri}}$, in the limit of $m \to \infty$, in Fig. 12. In the figures, each data point is the result of a separate extrapolation of the cumulants versus m. Upon careful numerical examination of the scaling behaviors of numerous ground states in the various phases, we were able to establish the scaling relation of $|\kappa_n| = \breve{a}_0 + \breve{a}_1 e^{-\breve{a}_2 m}, n = 2,4$, for ordered phase regions and make sense of the cumulant results in the $m \to \infty$ limit. These results show that κ_4 is comparatively large and negative when there is quasi-long-range magnetic ordering. Moreover, κ_2 is large and positive for quasi-LROs (see 120° and columnar phase regions in Fig. 12). This is in contrast to the behavior near phase transitions, and within the topological and algebraic spin liquids, where we were not able to find an appropriate analytical fit for the cumulants in the $m \to \infty$ limit, as they behave irregularly or quickly decay to numerically vanishing values. A likely reason for this is that for a magnetically

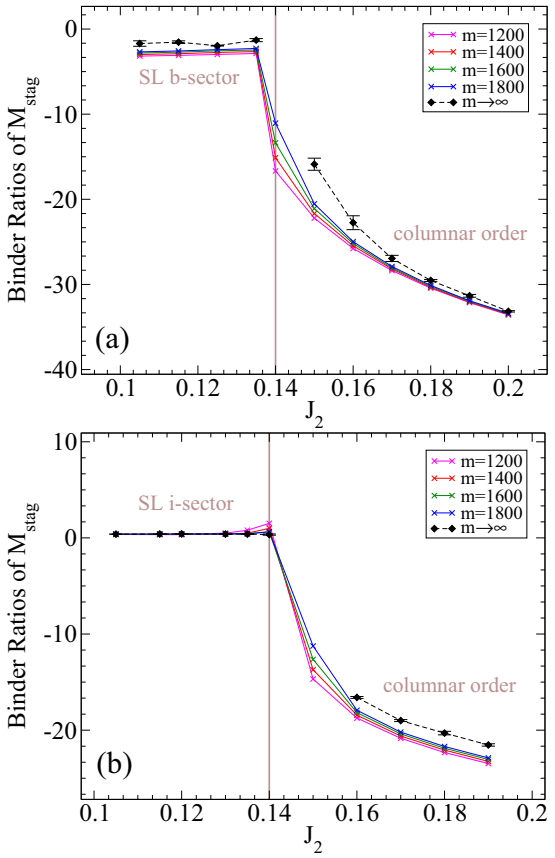

FIG. 13. iDMRG results for the Binder ratios, $U_r(m)$, Eq. (30), of M_{stag}, Eq. (27), in the vicinity of the topological SL and the columnar phase regions of the THM on (a) YC10 and (b) YC8 structures. Black diamonds denote $U_r(m \to \infty)$, i.e., extrapolations of Binder ratios according to Eq. (31) to the $m \to \infty$ limit. Brown stripes are the best estimate for the phase transition based on the discontinuity of the dashed line, $U_r(m \to \infty)$, for the larger system size, part (a).

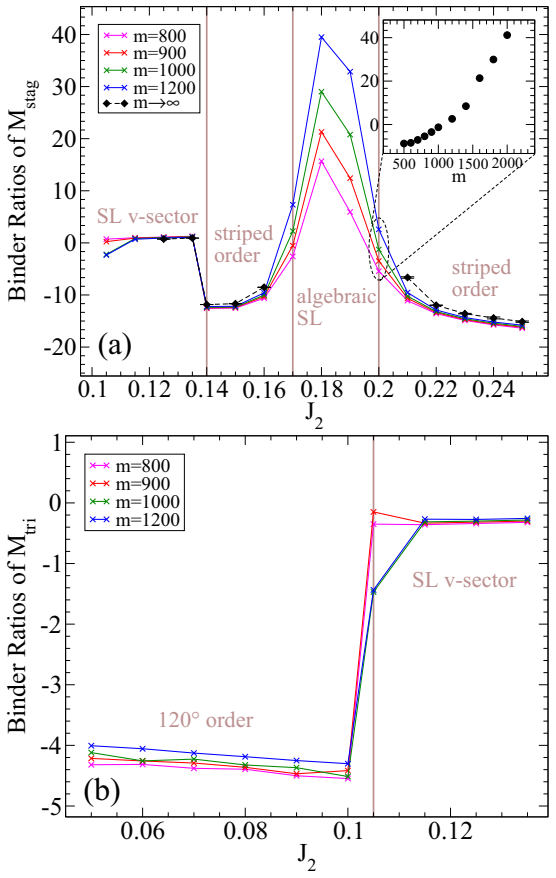

FIG. 14. iDMRG results for the Binder ratios, $U_r(m)$, Eq. (30), of (a) M_{stag}, Eq. (27), and (b) M_{tri}, Eq. (28), of the THM on YC6 systems. In part (a), black diamonds denote $U_r(m \to \infty)$, i.e., the the extrapolation of the of Binder ratio according to Eq. (31) toward the $m \to \infty$ limit. Furthermore, the inset shows the individual $U_r(M_{\text{stag}})$ at $J_2 = 0.2$. Brown stripes are the best estimate for the phase transition based on the discontinuities or rapid changes in U_r.

ordered, SU(2) $S = 0$ ground state, the moments $\mathbf{M}^{[k]}$ acquire a set of equally weighted nonzero values from the limited number of recovered (purely) TOS levels by iDMRG (see below). In such a case, the distribution function would resemble a discrete uniform distribution with very large and negative κ_4, and large and positive κ_2. However, for disordered states with no symmetry breaking in the thermodynamic limit, the distribution function is expected to resemble the normal distribution centered around zero magnetization, which has vanishing κ_4. For $\kappa_2(m \to \infty)$, in Fig. 12(a), we display in bold the boundaries where we were not able to extrapolate to $m \to \infty$. These are quite close to the phase transitions indicated by fDMRG, Fig. 9 (except for the YC6 structure, where we find an additional ASL phase), which supports the validity of the iDMRG cumulant method. The same behavior was observed for $\kappa_4(m \to \infty)$, indicated by the black dashed lines in Fig. 12(b). In addition, the extremely large (negative) values of $\kappa_4(m \to \infty)$ are consistent with our interpretation.

Our attempts to pinpoint the phase transitions of the THM on infinite cylinders, using U_r, is presented in Figs. 13 and 14. Based on these results, we argue that $U_r(m)$, as the ratio between $\kappa_4(m)$ and $\kappa_2(m)$, scaled with $\xi(m)$, regularly extrapolates to a finite value in the $m \to \infty$ limit everywhere, except close to (or on) a phase transition, or when the wave functions are noninjective (cf. Sec. V). Careful numerical examination suggests that the Binder ratios scale with a saturating behavior similar to the cumulants,

$$U_r = \check{b}_0 + \check{b}_1 e^{-\check{b}_2 m}. \tag{31}$$

In Fig. 13, we observe that in the topological SL phase region, $U_r(m)$ has a comparatively small value, as expected for nonmagnetic phases with $\gamma_4 \to 0$. In addition, when there is magnetic ordering, $U_r(m)$ converges to a finite, negative value, while it appears different m-curves tend to group together. The latter should be due to the fact that the iMPS magnetic orders are quantum critical states with an U_r independent from L_{eff}. Furthermore, for the ASL phase of YC6 structures [see Fig. 14(a)], very close to the expected phase transition points from the short-range correlation data, Fig. 8, and within the entire ASL phase region, U_r diverges with m [e.g., see the inset of Fig. 14(a)], where it is impossible to extrapolate to a finite $U_r(\infty)$. In the immediate vicinity of the transition from the 120° to topological spin liquid [cf.

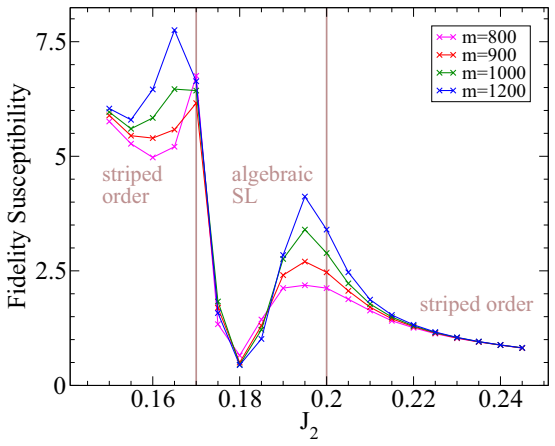

FIG. 15. iDMRG results for the fidelity susceptibility, χ_F^{approx}, Eq. (32), of the THM on YC6 systems. Brown stripes are the predicted phase transitions based on Fig. 14(a) results.

Fig. 14(b)], it was not possible to employ Eq. (31) due to unavoidable noninjectivity of the wave functions. However, we suggest that the fixed-m results are rather reliable and can be used to estimate a phase transition. Overall, we locate critical points of the THM from the discontinuities of $U_r(m \to \infty)$ lines (i.e., where there is no extrapolation possible) or when there is a significant kink in fixed-m data. Based on this approach, we estimate the phase transition points of $J_2 = 0.105(5)$ between the 120° and topological spin liquid states using YC6 results of Fig. 14(b), $J_2 = 0.140(5)$ between topological SL and columnar states using YC10 results of Fig. 13(a) [YC8 results of Fig. 13(b) would estimate a transition very close to this point, so we have based the final prediction on the larger-width data], and transition points of $J_2 = 0.140(5),0.170(5),0.200(5)$ encapsulating the ASL and columnar states using YC6 results of Fig. 14(a). To further validate U_r accuracy in estimating the transitions in case of YC6 structures, we also provide a numerical approximation for the *fidelity susceptibility* [118],

$$\chi_F^{\text{approx}} = \frac{1 - |\langle\psi_0(J_2)|\psi_0(J_2 + \delta J_2)\rangle|^2}{\delta J_2^2}, \qquad (32)$$

in Fig. 15, where we set $\delta J_2 = 0.05$. The fidelity susceptibility is known to be well-behaved and small when away from a phase boundary, but can diverge at a transition. It is clear from the figure that the diverging peaks of χ_F^{approx} (considering their tendency to lean toward the right) are happening relatively close to the predicted phase transitions from the Binder ratio results of Fig. 14(a).

VIII. NUMERICAL TOOLS II: 'TOS COLUMNS' IN THE MOMENTUM-RESOLVED ENTANGLEMENT SPECTRUM

The entanglement between the partitions of a quantum system is encoded in the spectrum of the entanglement Hamiltonian, $H_E = -\ln(\tilde{\rho})$, i.e., $\{-\ln(\lambda_i)\}$, which is known as the ES and commonly presented using energy-level arrangements analogous to an energy spectrum. $\{-\ln(\lambda_i)\}$ can be labeled using any global-symmetry quantum number to extract more information on the symmetry nature of the state (as long as the corresponding symmetry is preserved on the bipartite cut). H_E maintains the symmetries of a cylindrical wave function, however, there may exist some symmetries that are *not* explicitly preserved by the *Ansatz* due to the mapping of the 2D model onto an MPS chain. Nevertheless, one can still diagonalize such a symmetry operator in the "auxiliary" basis (i.e., the basis that diagonalizes H_E) to create a new set of good quantum numbers (see Refs. [63,64,85] for some examples). When the SU(2)-symmetry is preserved in the calculation, the obvious choice for the labels is the spin S quantum number (belonging to a single partition of the system). We refer to an H_E spectrum that is plotted against S (where no other label exists) as the *spin-resolved* ES. Kolley *et al.* [63] showed that the spin-resolved ES of a magnetically ordered state on finite-length cylinders shows signatures of symmetry-breaking in the thermodynamic limit. This emerges from a key finding: the realization [63,106,119] that the *low-energy* part of the ES of magnetic orders exhibits a specific type of grouped levels, known as the entanglement-spectrum TOS (also referred to as "quasidegenerate joint states"), closely resembling the low-lying levels in the energy spectrum, known as the Anderson TOS levels [10,20,72] (also referred to as the "Pisa tower" structure or the "thin spectrum"), which is considered as clear-cut evidence for the existence of *true* LROs on finite lattices. Kolley *et al.* established that, similar to the energy spectrum, for a fixed S-sector, entanglement-spectrum TOS levels are well-separated from the denser rest of the spectrum and the lowest energy levels of the ES, immediately above the TOS levels, are spin-wave states (Nambu-Goldstone modes). In this paper, we are interested in exploiting both the S quantum numbers [SU(2) is explicitly preserved in the iDMRG calculations], and the momenta in the cylinder Y direction, k, i.e., the complex phase of the eigenvalues of the reduced T_y operator, where T_y is the translation by one site in Ydirection; we can decompose the operator in the same way as the Schmidt decomposition of the wave function [54], $T_y = T_y^L \otimes T_y^R$, where T_y^L and T_y^R are the reduced operators and maintain the unitary property of the original operator. T_y is *not* preserved exactly in the calculations due to the MPS mapping on the cylinder, Fig. 1, but it can be diagonalized straightforwardly [93]. We refer to an H_E spectrum that is plotted against k and additionally labeled by S, as the momentum-resolved ES, $\{-\ln(\lambda_n[k_n, S_n])\}$. For a system with PBC in Y direction, dihedral symmetry implies that $T_y^{L_y} = I$. As a result, the allowed momentum spacing is as $\Delta k_n = \frac{2\pi n}{L_y}$ for $n = 0, 1, \ldots, L_y - 1$. We notice that k_0, the momentum of the lowest ES level, is not fixed due to the possibility of inserting a shift in the expectation value of T_y (one needs to first fix k_0, then measure the rest of the momenta in respect to it; physically only Δk_n matters here, see also Refs. [92,93]). The study of momentum-resolved forms of the ES is now finding a place in literature of the low-dimensional quantum magnets. Another key breakthrough was the realization that such ES can be used to fully classify anyonic sectors of chiral [64] and Z_2-gauge [120] topological orders on infinite cylinders [85]. Below, we argue that the symmetry-breaking can be recognized and characterized using the momentum-resolved ES, which shows the symmetry properties even more robustly than the spin-resolved ES.

Upon careful examination of the momentum-resolved ES of the magnetic orders in the THM on infinite cylinders and noticing the underlying symmetries of the sublattices, we find that the spectrum contains exactly N_s (number of the ground-state sublattices) column-like structures, which are the low-lying component TOS levels, independent of the system width. We shall refer to these particular patterns as "TOS columns." The appearance of TOS columns is due to that, as previously discussed, the TOS levels are clear features in the low-lying ES. These columns also have a momentum structure. Consider an ideal magnetic order that consists of N_s fully FM sublattices, represented as $\{\tilde{\mathbf{S}}_1,\tilde{\mathbf{S}}_2,\ldots,\tilde{\mathbf{S}}_{N_s}\}$ ($L_y = 0 \mod N_s$) in a big-S notation of the spins. The SU(2)-symmetric ground state is, of course, the $S_{\text{total}} = 0$-singlet, constructed by adding all spins, $||\tilde{\mathbf{S}}_1,\tilde{\mathbf{S}}_2,\ldots,\tilde{\mathbf{S}}_{N_s};0\rangle$ in a reduced dimension basis notation (see, for example, Ref. [121]). Importantly, this is the true ground state of the effective Hamiltonian of $H_{\text{eff}} \propto \frac{1}{\sqrt{L}}\mathbf{S}^2_{\text{total}}$ describing purely the TOS levels [63]. The only nontrivial sets of unitary symmetry operations that are allowed to act on the $S_{\text{total}} = 0$-singlet and leave a Heisenberg-type Hamiltonian between the sublattices unchanged (sublattices should be still arranged on the physical lattice), can be written as the cyclic translations of sublattices, T_ν, where ν is the number of sublattices that will be shifted (for example to the right). One can then write

$$\begin{aligned} T_{\nu=N_s}\ ||\ \mathbf{S}_1,\mathbf{S}_2,\mathbf{S}_3,\ldots,\mathbf{S}_{N_s};0\rangle &= \\ T^{N_s}_{\nu=1}\ ||\ \mathbf{S}_1,\mathbf{S}_2,\mathbf{S}_3,\ldots,\mathbf{S}_{N_s};0\rangle &= \\ ||\ \mathbf{S}_1,\mathbf{S}_2,\mathbf{S}_3,\ldots,\mathbf{S}_{N_s};0\rangle. & \end{aligned} \tag{33}$$

There are obviously only N_s distinct values that ν can take, including the identity operator. Equation (33) already implies that the TOS levels can only acquire lattice momenta of $k^{\text{TOS}}_\nu = \frac{2\pi\nu}{N_s}$ for $\nu = 0,1,\ldots,N_s-1$, between the equal or greater group of general ES momenta, k_n. The only complication emerges from the distribution pattern of n' TOS levels between N_s momenta for a fixed S sector. To clarify this, let us focus on the more general case of $n' > N_s$ and choose the momentum of the lowest ES level to be $k^{\text{TOS}}_0[S=0] = 0$, presumably, corresponding to the action of I on the sublattices (chosen differently in Fig. 17). Trivially, all other $(n'-1)$ levels should arrange symmetrically in respect to $k^{\text{TOS}}_0[S=0]$ (there is no relative net momentum). So, they can either, altogether, fill the zero-momentum state on top of $k^{\text{TOS}}_0[S=0]$ or occupy $\pm k_\nu$ ($\nu \neq 0$) states around it. The former is *not* possible, due to the fact that T_ν ($\nu \neq 0$) and I posses a distinct set of eigenvalues and therefore produce different momenta (this can be easily observed by writing the bipartite Schmidt decomposition of the $S_{\text{total}} = 0$-singlet state and switch to the basis of fixed-S states for L or R partition to reveal distinct eigenspectra of T_ν and I). In addition, we notice that some states appearing in a TOS column are *not* essentially TOS levels. This is partly due to the fact that the non-TOS levels are also allowed to fill k^{TOS}_ν states, and partly because in an MPS representation, there is always a *fixed* number of states kept and consequently, only the first few TOS levels of H_{eff} will be recovered. Nevertheless, such initial states (having a clear gap to the higher levels) certainly follow the TOS level counting as governed by the degree of symmetry-breaking in the thermodynamic limit. That is, for a state that *fully* breaks SU(2) symmetry (e.g., the 120° order), there are $N^{\text{TOS}}_S = (2S+1)$ levels grouped together, and for a state that *partially* breaks the SU(2)-symmetry down to U(1) (e.g., the columnar order), there is only $N^{\text{TOS}}_S = 1$ level per each fixed S sector (*not* counting the degeneracy that comes from the SU(2) quantum numbers themselves; the overall degeneracy of the ES levels is always $(2S+1)N^{\text{TOS}}_S$, see Refs. [63,93] for more details). We discover another striking feature in the momentum-resolved ES of symmetry-broken phases, however, this time for the states between the TOS columns: the first few Nambu-Goldstone modes exhibit *sine-like* dispersion patterns (as in the energy spectrum), if L_y chosen to be large enough.

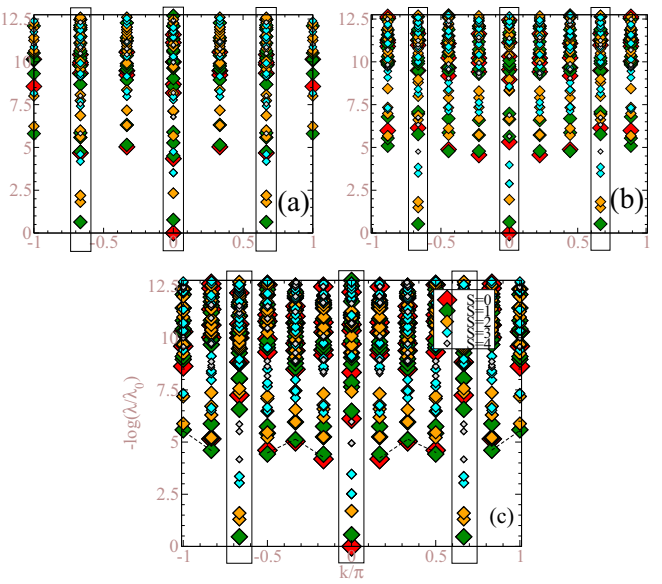

FIG. 16. iDMRG momentum-resolved ES of the 120° order, $J_2 = -1.0$, for (a) YC6, (b) YC9, and (c) YC12 structures of the THM vs Y-direction momenta (the reference momentum is fixed to $k^{\text{TOS}}[\lambda_0] = 0$). Boxes emphasize TOS columns at the unique momenta of $k^{\text{TOS}}_\nu = -\frac{2\pi}{3},0,\frac{2\pi}{3}$. In part (c), dashed lines are guides to the eyes and connect the Nambu-Goldstone modes of the ES for the first few levels on the top of the TOS levels.

In Fig. 16, we present the momentum-resolved ES of the 120° order on different width of the YC structure (for more visibility, we have limited the display of the ES levels to $S_{\max} = 4$ in all ES figures of this section). The presence of *three* characterizing TOS columns is clear for all system widths, consistent with the theory for a $N_s = 3$ state. The low-lying levels inside the TOS columns (purely TOS levels) have a clear gap to the higher levels, which qualitatively observed to converge to a finite value, linearly with $\frac{1}{L_y}$, at the thermodynamic limit [93]. The number of low-lying levels in the TOS columns agree with the full SU(2)-symmetry breaking in the thermodynamic limit. That is, $N^{\text{TOS}}_S = (2S+1)$ for all $S = 0,1,2,3,4$, as previously observed by Kolley *et al.* [63]. For low-lying Nambu-Goldstone modes between the TOS columns, we suggest the triangular-shape dispersion patterns of Fig. 16(c) are signs for the formation of sinelike structures, however, due to relatively small size of L_y, the k_n-resolution does not suffice to discern more details.

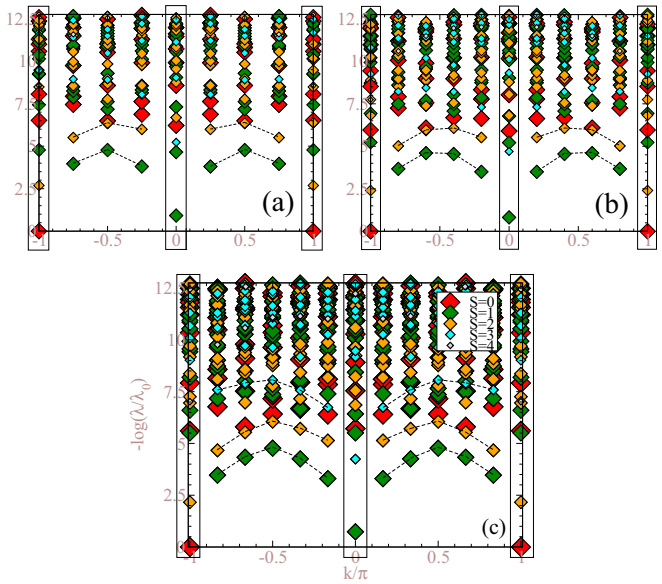

FIG. 17. iDMRG momentum-resolved ES of the columnar order, $J_2 = 0.5$, for (a) YC8, (b) YC10 and (c) YC12 structures of the THM vs Y-direction momenta (the reference momentum is fixed as $k^{\mathrm{TOS}}[\lambda_0] = \pm\pi$). Boxes emphasize TOS columns at the unique momenta of $k_y^{\mathrm{TOS}} = 0,\pi$. Dashed lines are guides to the eyes and connect the Nambu-Goldstone modes of the ES for the first few levels on the top of the TOS levels.

In Fig. 17, we present the momentum-resolved ES of the columnar order for different widths of the YC structure. The presence of *two* characterizing TOS columns (note that $k^{\mathrm{TOS}}[\lambda_0] = \pm\pi$ columns are the same) is clear for all system widths, as predicted by the theory for an $N_s = 2$ state. As before, the low-lying levels inside the TOS columns have a clear gap to the higher levels and observed to converge to a finite value, linearly with $\frac{1}{L_y}$, at the thermodynamic limit [93]. The partial breaking of SU(2) to U(1) symmetry can be confirmed by the level counting of $N_S^{\mathrm{TOS}} = 1$ for low-lying $S = 0,1,2,3,4$-levels in the TOS columns. A sinelike dispersion pattern for the low-lying levels between the TOS columns is apparent, at least, for the larger $L_y = 12$ system, Fig. 17(c).

In Fig. 18, we present the momentum-resolved ES of an ASL state on an $L_y = 6$ cylinder. Clearly, there is no signature for the presence of TOS columns, which suggests the nonmagnetic nature of the phase. In addition, we observe *no* nontrivial degeneracy of low-lying ES levels. So, there exist *no* fractionalization of symmetries to identify SPT and/or some intrinsic topological ordering with anyonic excitations (see also Ref. [85]).

IX. TIME-REVERSAL SYMMETRY-BREAKING AND THE ROBUSTNESS OF THE TOPOLOGICAL PHASE AGAINST THE CHIRALITY

The existence of time reversal symmetry is a key feature of H_{J_2}, Eq. (1). A chiral ground state spontaneously breaks time-reversal, τ, and parity reflection, P, symmetry, but respects the combined $P\tau$ symmetry. After consistent numerical

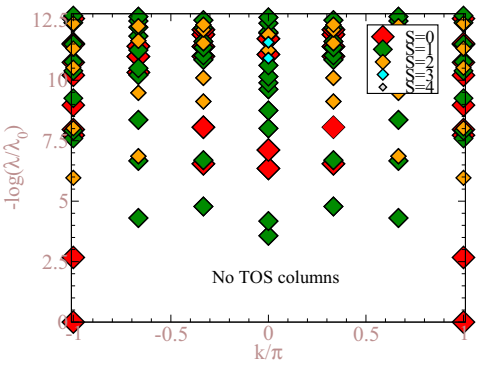

FIG. 18. iDMRG momentum-resolved ES of an ASL state, $J_2 = 0.185$, for the YC6 structure of the THM versus Y-direction momenta (the reference momentum is fixed as $k[\lambda_0] = \pm\pi$).

observations of a nonmagnetic phase in the J_1-J_2 THM phase diagram (cf. Secs. I and III), the natural question is, whether the new state stabilizes due to SSB of τ, which would result in an CSL. For a scenario in which the true ground state in the SL phase region is Z_2 topologically ordered (advocated by DMRG results [76,77,85]), we already investigated [85] the chirality of anyonic sectors in detail, using a direct measurement of the τ-operator expectation values and calculating a scalar chiral order parameter,

$$O_\chi = \frac{1}{L_u}\sum_{\langle i,j,k\rangle}(\mathbf{S}_i \times \mathbf{S}_j)\cdot\mathbf{S}_k, \tag{34}$$

where $\langle i,j,k\rangle$ represent an NN triangular plaquette and the sum goes over the wave-function unit cell. We discovered that the topological sectors are all τ-symmetric as the O_χ values are observed to be small and decreasing rapidly to numerically vanishing magnitudes at the thermodynamic limit of $m \to \infty$ (furthermore, $\hat{\mathrm{b}}$ and $\hat{\mathrm{f}}$-sector are fractionalizing time-reversal symmetry). However, Hu *et al.* [77] determined the $\hat{\imath}$-sector ground state as strongly prone to the chirality by adding directional ($\mathbf{a}_{\pm 60^\circ}$-axis) anisotropy to the Hamiltonian. This is, in part, leading another question of our interest: is the SL phase robust against perturbing H_{J_2} with a term that explicitly breaks the τ symmetry and forms a chiral long-range order? To answer this question, one can study the J_1-J_2-J_χ model,

$$H_\chi = H_{J_2} + J_\chi\sum_{\langle i,j,k\rangle}(\mathbf{S}_i \times \mathbf{S}_j)\cdot\mathbf{S}_k, \tag{35}$$

where $\langle i,j,k\rangle$ indicates the sum over all NN triangular plaquettes in a Hamiltonian unit cell. The phase diagram of H_χ is previously studied using variational QMC [87] and ED [84] techniques, however, no clear result has emerged on the nature of the $J_\chi \to 0$ limit. To shed some lights on this matter, in this section we study the response of the YC8-$\hat{\imath}$ ground states [85] to the chiral field by adiabatically adding a J_χ term to H_{J_2}, as in Eq. (35), and finding new ground states using the SU(2)-symmetric iMPS and iDMRG methods.

We present our results for the extrapolated O_χ in the thermodynamic limit of $m \to \infty$ in Fig. 19. We notice that, within our resolution, upon varying J_χ, there is at least one (significant) point exposed to nonzero chiral perturbations, but

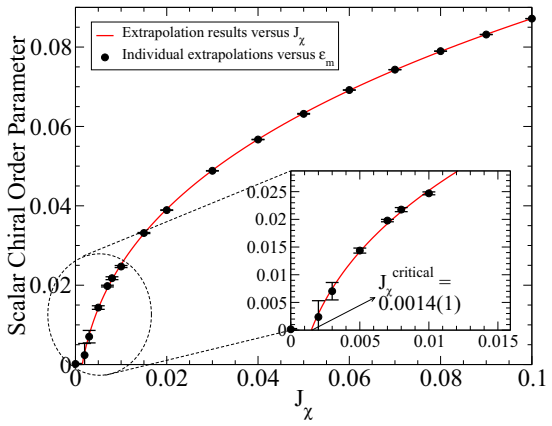

FIG. 19. iDMRG results for the scalar chiral order parameter, O_χ, Eq. (34), vs J_χ for the ground states of H_χ, Eq. (35), constructed from a YC8-î sector. Each data point represents a $O_\chi[m \to \infty, J_\chi]$, which is the result of a separate extrapolation on individual O_χ vs ε_m toward the thermodynamic limit of $\varepsilon_m \to 0$ ($m \to \infty$). The red line is our attempted fit of $\tilde{b}_0 + \tilde{b}_1 J_\chi^{\tilde{b}_2}$ to the black circles, excluding the first two J_χ points (where the chirality is zero within the error bars), which is used to estimate the phase transition when $O_\chi[m \to \infty, J_\chi^{\text{critical}}] = 0$. A zoom-in plot is presented in the inset, as a guide to the eyes.

has negligible $O_\chi(m \to \infty)$ within the error-bars. This means that the topological SL phase is robust against chirality and one needs to provide τ-symmetry-breaking terms larger than a finite-value, namely J_χ^{critical}, to impose a chiral ground state. To further predict this small J_χ^{critical}, we applied a fit of $\tilde{b}_0 + \tilde{b}_1 J_\chi^{\tilde{b}_2}$ to the data and find $J_\chi^{\text{critical}} = (-\frac{b_0}{b_1})^{\frac{1}{b_2}} = 0.0014(1)$. These results also suggest the existence of a *second-order* phase transition toward the CSL phase. This is consistent with the suggestion from Wietek and Läuchli [84], and may clarify the results of Hu *et al.* [87], where it is unclear if O_χ would be zero or not in the $J_\chi \to 0$ limit.

X. CONCLUSION

We have presented comprehensive results for the phase diagram of the J_1-J_2 Heisenberg model on triangular lattices, using infinite-length YC structures. Using the Binder ratio of the magnetization order parameter, U_r, Eq. (31), and TOS columns of the momentum-resolved ES, we have obtained phase boundaries and characterized the nature of the symmetry breaking magnetic order. We found that the Binder ratio reliably detects phase boundaries between magnetically ordered states, even when using SU(2) symmetry, where the order parameter itself is zero by construction. We identified the 120°-ordered ground state as a three-sublattice LRO with full SU(2)-symmetry-breaking in the thermodynamic limit; the columnar-ordered ground state as a two-sublattice LRO with partial SU(2)-symmetry-breaking in the thermodynamic limit, and confirm the nonmagnetic nature of the SL states on infinite cylinders of widths up to 12 sites. In addition, we have discovered the stabilization of a new ASL phase, with power-law correlations, for width-6 infinite cylinders. We have pinpointed the phase transitions between the infinite cylinder's ground states of the THM, precisely, using the Binder ratios. The transitions are relatively close to the phase boundaries found from the direct measurements of the local order parameters using fDMRG on $L_y = 3,4,5,6$ cylinders, and short-range correlations and fidelity susceptibility measurements from iDMRG calculations. In addition, for the columnar order, we have numerically proved that the entropies consistently obey $S_{\text{EE}} = a_0(L_y) + (\alpha_0 + \alpha_1 L_y)\ln(\xi)$, a mixture of the area-law and quantum critical behavior, as expected for the magnetic phases built by the inherently one-dimensional SU(2)-symmetric iMPS *Ansatz*. To the best of our knowledge, a set of numerical tools to efficiently distinguish and classify LROs were previously absent in the SU(2)-symmetric iDMRG literature. Considering the advantages of SU(2)-symmetric calculations, we suggest that the proposed methods can be applied widely to detect symmetry broken states using the iMPS.

Finally, to unravel the true nature of time-reversal symmetry breaking in the topological SL, we have investigated the robustness of YC8-î sector under perturbing H_{J_χ} with a chiral term, Eq. (35) (it was previously suggested [77] that YC8-î states are prone to become chiral under applying bond anisotropies to the Hamiltonian). The results of the scalar chiral order parameter, $O_\chi(m \to \infty)$, versus J_χ can be fitted using $\tilde{b}_0 + \tilde{b}_1 J_\chi^{\tilde{b}_2}$ with high accuracy, and show the existence of a continuous phase transition to the CSL phase at small, but nonzero, $J_\chi^{\text{critical}} = 0.0014(1)$. Therefore, for finite-width cylinders, the topological state of the THM is time-reversal symmetric, and not a chiral topological liquid.

Note added in proof. After completing this work, a related paper [122] appeared in which the authors study the phase diagram of the J_1-J_2-J_χ model, Eq. (35), on finite-L_x cylinders using the SU(2)-symmetric fDMRG algorithm. In agreement to Sec. IX results, Gong *et al.* find a smooth phase transition from J_1-J_2 SL to a CSL at a small but finite chiral coupling strength ($J_\chi^{\text{critical}} \approx 0.02$ for $J_2 = 0.1$).

ACKNOWLEDGMENTS

The authors would like to thank Jason Pillay for useful discussions. This work has been supported by the Australian Research Council (ARC) Centre of Excellence for Engineered Quantum Systems, grant CE110001013. I.P.M. also acknowledges support from the ARC Future Fellowships scheme, FT140100625.

[1] W. Heisenberg, Zur theorie des ferromagnetismus, Z. Phys. **49**, 619 (1928).

[2] U. Schollwöck, J. Richter, D. J. J. Farnell, and R. F. Bishop, editors, *Quantum Magnetism*, 1st ed. Lecture Notes in Physics Vol. 645 (Springer-Verlag, Berlin Heidelberg, 2004). See Chap. 1 (2) for an introduction to one-dimensional (two-dimensional) quantum magnetism, Chapter 4 for the details on the Heisenberg-type magnets, and Chaps. 5 and 7 for some examples on the highly-accurate numerical simulations.

[3] A. Auerbach, *Interacting Electrons and Quantum Magnetism*, Lecture Notes in Physics, 1st ed. (Springer-Verlag, New York, 1994).

[4] S. Sachdev, *Quantum Phase Transitions* (Cambridge University Press, 2011). See Chaps. 7, 8, and 19.

[5] H. Bethe, Zur theorie der metalle, Z. Phys. **71**, 205 (1931).

[6] M. Karbach, K. Hu, and G. Müller, Introduction to the Bethe *Ansatz* II, arXiv:cond-mat/9809163.

[7] N. D. Mermin and H. Wagner, Absence of Ferromagnetism or Antiferromagnetism in One- or Two-Dimensional Isotropic Heisenberg Models, Phys. Rev. Lett. **17**, 1133 (1966).

[8] P. C. Hohenberg, Existence of long-range order in one and two dimensions, Phys. Rev. **158**, 383 (1967).

[9] J. Frohlich and E. H. Lieb, Phase transitions in anisotropic lattice spin systems, Commun. Math. Phys. **60**, 233 (1978).

[10] P. W. Anderson, An approximate quantum theory of the antiferromagnetic ground state, Phys. Rev. **86**, 694 (1952).

[11] J. Oitmaa and D. D. Betts, The ground state of two quantum models of magnetism, Can. J. Phys. **56**, 897 (1978).

[12] D. A. Huse and V. Elser, Simple Variational Wave Functions for Two-Dimensional Heisenberg Spin-1/2 Antiferromagnets, Phys. Rev. Lett. **60**, 2531 (1988).

[13] D. A. Huse, Ground-state staggered magnetization of two-dimensional quantum Heisenberg antiferromagnets, Phys. Rev. B **37**, 2380 (1988).

[14] T. Kennedy, E. H. Lieb, and B. S. Shastry, Existence of Néel order in some spin-1/2 Heisenberg antiferromagnets, J. Stat. Phys. **53**, 1019 (1988).

[15] J. D. Reger and A. P. Young, Monte Carlo simulations of the spin-(1/2) Heisenberg antiferromagnet on a square lattice, Phys. Rev. B **37**, 5978 (1988).

[16] E. J. Neves and J. F. Perez, Long range order in the ground state of two-dimensional antiferromagnets, Phys. Lett. A **114**, 331 (1986).

[17] T. Kennedy, E. H. Lieb, and B. S. Shastry, The XY Model has Long-Range Order for All Spins and All Dimensions Greater Than One, Phys. Rev. Lett. **61**, 2582 (1988).

[18] K. Kubo and T. Kishi, Existence of Long-Range Order in the XXZ Model, Phys. Rev. Lett. **61**, 2585 (1988).

[19] Y. Okabe and M. Kikuchi, Quantum monte carlo simulation of the spin 1/2 XXZ model on the square lattice, J. Phys. Soc. Jpn. **57**, 4351 (1988).

[20] C. Lhuillier, Frustrated quantum magnets, arXiv:cond-mat/0502464.

[21] D. J. J. Farnell, O. Götze, J. Richter, R. F. Bishop, and P. H. Y. Li, Quantum $s = \frac{1}{2}$ antiferromagnets on archimedean lattices: The route from semiclassical magnetic order to nonmagnetic quantum states, Phys. Rev. B **89**, 184407 (2014).

[22] L. Néel, Propriétées magnétiques des ferrites; férrimagnétisme et antiferromagnétisme, Annales de Physique (Paris) **12**, 137 (1948).

[23] L. D. Landau, On the theory of the phase transitions I, Phys. Z. Sowjetunion **11**, 26 (1937); On the theory of the phase transitions II, Phys. Z. Sowjetunion **11**, 545 (1937); English translations available at *Collected Papers of L. D. Landau* by D. Ter Haar (Elsevier, Pergamon imprint, 2013).

[24] L. D. Landau and V. L. Ginzburg, On the theory of superconductivity, Zh. Eksp. Teor. Fiz., **20**, 1064 (1950); English translation available at *Collected Papers of L. D. Landau* by D. Ter Haar (Elsevier, Pergamon imprint, 2013).

[25] A. M. Tsvelik, *Quantum Field Theory in Condensed Matter Physics* (Cambridge University Press, 2007).

[26] Z.-C. Gu and X.-G. Wen, Tensor-entanglement-filtering renormalization approach and symmetry-protected topological order, Phys. Rev. B **80**, 155131 (2009).

[27] F. Pollmann and A. M. Turner, Detection of symmetry-protected topological phases in one dimension, Phys. Rev. B **86**, 125441 (2012).

[28] F. Pollmann, A. M. Turner, E. Berg, and M. Oshikawa, Entanglement spectrum of a topological phase in one dimension, Phys. Rev. B **81**, 064439 (2010).

[29] F. Pollmann, E. Berg, A. M. Turner, and M. Oshikawa, Symmetry protection of topological phases in one-dimensional quantum spin systems, Phys. Rev. B **85**, 075125 (2012).

[30] A. M. Turner, F. Pollmann, and E. Berg, Topological phases of one-dimensional fermions: An entanglement point of view, Phys. Rev. B **83**, 075102 (2011).

[31] L. Balents, Spin liquids in frustrated magnets, Nature (London) **464**, 199 (2010).

[32] X. Chen, Z.-C. Gu, and X.-G. Wen, Local unitary transformation, long-range quantum entanglement, wave function renormalization, and topological order, Phys. Rev. B **82**, 155138 (2010).

[33] B. J. Powell and R. H. McKenzie, Quantum frustration in organic mott insulators: From spin liquids to unconventional superconductors, Rep. Prog. Phys. **74**, 056501 (2011).

[34] H. T. Diep, *Frustrated Spin Systems* (World Scientific, 2004).

[35] C. Lacroix, P. Mendels, and F. Mila, *Introduction to Frustrated Magnetism: Materials, Experiments, Theory*, Springer Series in Solid-State Sciences (Springer, Berlin Heidelberg, 2011).

[36] V. Kalmeyer and R. B. Laughlin, Equivalence of the Resonating-Valence-Bond and Fractional Quantum Hall States, Phys. Rev. Lett. **59**, 2095 (1987).

[37] X. G. Wen, F. Wilczek, and A. Zee, Chiral spin states and superconductivity, Phys. Rev. B **39**, 11413 (1989).

[38] X. G. Wen, Mean-field theory of spin-liquid states with finite energy gap and topological orders, Phys. Rev. B **44**, 2664 (1991).

[39] N. Read and S. Sachdev, Large-N Expansion for Frustrated Quantum Antiferromagnets, Phys. Rev. Lett. **66**, 1773 (1991).

[40] X.-G. Wen, Quantum orders and symmetric spin liquids, Phys. Rev. B **65**, 165113 (2002).

[41] X. G. Wen, *Quantum Field Theory of Many-Body Systems: From the Origin of Sound to an Origin of Light and Electrons*, Oxford Graduate Texts (Oxford University Press, Oxford, 2007).

[42] I. Affleck, T. Kennedy, E. H. Lieb, and H. Tasaki, Rigorous Results on Valence-Bond Ground States in Antiferromagnets, Phys. Rev. Lett. **59**, 799 (1987).

[43] I. Affleck, T. Kennedy, E. H. Lieb, and H. Tasaki, Valence bond ground states in isotropic quantum antiferromagnets, Commun. Math. Phys. **115**, 477 (1988).

[44] A. Yu. Kitaev, Fault-tolerant quantum computation by anyons, Ann. Phys. **303**, 2 (2003).

[45] A. Kitaev, Anyons in an exactly solved model and beyond, Ann. Phys. **321**, 2 (2006).

[46] A. Kitaev and C. Laumann, Topological phases and quantum computation, arXiv:0904.2771v1.

[47] S. R. White and D. A. Huse, Numerical renormalization-group study of low-lying eigenstates of the antiferromagnetic $S = 1$ Heisenberg chain, Phys. Rev. B **48**, 3844 (1993).

[48] S. Rommer and S. Östlund, Class of *Ansatz* wave functions for one-dimensional spin systems and their relation to the density matrix renormalization group, Phys. Rev. B **55**, 2164 (1997).

[49] S. Östlund and S. Rommer, Thermodynamic Limit of Density Matrix Renormalization, Phys. Rev. Lett. **75**, 3537 (1995).

[50] A. W. Sandvik, Computational studies of quantum spin systems, AIP Conf. Proc. **1297**, 135 (2010).

[51] S. R. White, Density Matrix Formulation for Quantum Renormalization Groups, Phys. Rev. Lett. **69**, 2863 (1992).

[52] S. R. White, Density-matrix algorithms for quantum renormalization groups, Phys. Rev. B **48**, 10345 (1993).

[53] I. P. McCulloch, From density-matrix renormalization group to matrix product states, J. Stat. Mech. (2007) P10014.

[54] U. Schollwöck, The density-matrix renormalization group in the age of matrix product states, Ann. Phys. **326**, 96 (2011).

[55] I. P. McCulloch, Infinite size density matrix renormalization group, revisited, arXiv:0804.2509.

[56] D. Perez-Garcia, F. Verstraete, M. M. Wolf, and J. I. Cirac, Matrix product state representations, Quantum Inf. Comput. **7**, 401 (2007).

[57] T. Koma and H. Tasaki, Symmetry breaking and finite-size effects in quantum many-body systems, J. Stat. Phys. **76**, 745 (1994).

[58] L. Tagliacozzo, T. R. de Oliveira, S. Iblisdir, and J. I. Latorre, Scaling of entanglement support for matrix product states, Phys. Rev. B **78**, 024410 (2008).

[59] V. Stojevic, J. Haegeman, I. P. McCulloch, L. Tagliacozzo, and F. Verstraete, Conformal data from finite entanglement scaling, Phys. Rev. B **91**, 035120 (2015).

[60] J. Eisert, M. Cramer, and M. B. Plenio, Colloquium: Area laws for the entanglement entropy, Rev. Mod. Phys. **82**, 277 (2010).

[61] A. Stuart, K. Ord, S. Arnold, A. O'Hagan, and J. Forster, *Kendalls Advanced Theory of Statistics* (Wiley, 2009). For details on the noncentral moments and the cumulants see Sec. 3.12 of Vol. 1: Distribution Theory.

[62] H. Li and F. D. M. Haldane, Entanglement Spectrum as a Generalization of Entanglement Entropy: Identification of Topological Order in Non-Abelian Fractional Quantum Hall Effect States, Phys. Rev. Lett. **101**, 010504 (2008).

[63] F. Kolley, S. Depenbrock, I. P. McCulloch, U. Schollwöck, and V. Alba, Entanglement spectroscopy of SU(2)-broken phases in two dimensions, Phys. Rev. B **88**, 144426 (2013).

[64] L. Cincio and G. Vidal, Characterizing Topological Order by Studying the Ground States on an Infinite Cylinder, Phys. Rev. Lett. **110**, 067208 (2013).

[65] P. W. Anderson, Resonating valence bonds: A new kind of insulator? Mater. Res. Bull. **8**, 153 (1973).

[66] P. Fazekas and P. W. Anderson, On the ground state properties of the anisotropic triangular antiferromagnet, Philos. Mag. **30**, 423 (1974).

[67] R. Deutscher and H. U. Everts, The $S = 1/2$ Heisenberg antiferromagnet on the triangular lattice: Exact results and spin-wave theory for finite cells, Z. Phys. B: Condens. Matter **93**, 77 (1993).

[68] L. Capriotti, A. E. Trumper, and S. Sorella, Long-Range Néel Order in the Triangular Heisenberg Model, Phys. Rev. Lett. **82**, 3899 (1999).

[69] T. Jolicoeur and J. C. Le Guillou, Spin-wave results for the triangular Heisenberg antiferromagnet, Phys. Rev. B **40**, 2727 (1989).

[70] Th. Jolicoeur, E. Dagotto, E. Gagliano, and S. Bacci, Ground-state properties of the $S = 1/2$ Heisenberg antiferromagnet on a triangular lattice, Phys. Rev. B **42**, 4800(R) (1990).

[71] A. V. Chubukov and T. Jolicoeur, Order-from-disorder phenomena in Heisenberg antiferromagnets on a triangular lattice, Phys. Rev. B **46**, 11137 (1992).

[72] B. Bernu, P. Lecheminant, C. Lhuillier, and L. Pierre, Exact spectra, spin susceptibilities, and order parameter of the quantum Heisenberg antiferromagnet on the triangular lattice, Phys. Rev. B **50**, 10048 (1994).

[73] S. R. White and A. L. Chernyshev, Neél Order in Square and Triangular Lattice Heisenberg Models, Phys. Rev. Lett. **99**, 127004 (2007).

[74] R. Kaneko, S. Morita, and M. Imada, Gapless spin-liquid phase in an extended spin 1/2 triangular Heisenberg model, J. Phys. Soc. Jpn. **83**, 093707 (2014).

[75] P. H. Y. Li, R. F. Bishop, and C. E. Campbell, Quasiclassical magnetic order and its loss in a spin-$\frac{1}{2}$ Heisenberg antiferromagnet on a triangular lattice with competing bonds, Phys. Rev. B **91**, 014426 (2015).

[76] Z. Zhu and S. R. White, Spin liquid phase of the $s = \frac{1}{2}J_1 - J_2$ Heisenberg model on the triangular lattice, Phys. Rev. B **92**, 041105 (2015).

[77] W.-J. Hu, S.-S. Gong, W. Zhu, and D. N. Sheng, Competing spin-liquid states in the spin-$\frac{1}{2}$ Heisenberg model on the triangular lattice, Phys. Rev. B **92**, 140403 (2015).

[78] Y. Iqbal, W.-J. Hu, R. Thomale, D. Poilblanc, and F. Becca, Spin liquid nature in the Heisenberg $J_1 - J_2$ triangular antiferromagnet, Phys. Rev. B **93**, 144411 (2016).

[79] S. N. Saadatmand, B. J. Powell, and I. P. McCulloch, Phase diagram of the spin $-\frac{1}{2}$ triangular $J_1 - J_2$ Heisenberg model on a three-leg cylinder, Phys. Rev. B **91**, 245119 (2015).

[80] E. Dagotto and A. Moreo, Phase Diagram of the Frustrated Spin-1/2 Heisenberg Antiferromagnet in 2 Dimensions, Phys. Rev. Lett. **63**, 2148 (1989).

[81] J. E. Hirsch and S. Tang, Two-dimensional Heisenberg antiferromagnet with next-nearest-neighbor coupling, Phys. Rev. B **39**, 2887 (1989).

[82] L. O. Manuel and H. A. Ceccatto, Magnetic and quantum disordered phases in triangular-lattice Heisenberg antiferromagnets, Phys. Rev. B **60**, 9489 (1999).

[83] R. V. Mishmash, J. R. Garrison, S. Bieri, and C. Xu, Theory of a Competitive Spin Liquid State for Weak Mott Insulators on the Triangular Lattice, Phys. Rev. Lett. **111**, 157203 (2013).

[84] A. Wietek and A. M. Läuchli, Chiral spin liquid and quantum criticality in extended $S = 1/2$ Heisenberg models on the triangular lattice, Phys. Rev. B **95**, 035141 (2017).

[85] S. N. Saadatmand and I. P. McCulloch, Symmetry fractionalization in the topological phase of the spin-$\frac{1}{2}$ J_1-J_2 triangular Heisenberg model, Phys. Rev. B **94**, 121111 (2016).

[86] L. E. Svistov, A. I. Smirnov, L. A. Prozorova, O. A. Petrenko, L. N. Demianets, and A. Y. Shapiro, Quasi-two-dimensional antiferromagnet on a triangular lattice $RbFe(MoO_4)_2$, Phys. Rev. B **67**, 094434 (2003).

[87] W.-J. Hu, S.-S. Gong, and D. N. Sheng, Variational monte carlo study of chiral spin liquid in quantum antiferromagnet on the triangular lattice, Phys. Rev. B **94**, 075131 (2016).

[88] S. R. White, Density matrix renormalization group algorithms with a single center site, Phys. Rev. B **72**, 180403 (2005).
[89] C. Hubig, I. P. McCulloch, U. Schollwöck, and F. A. Wolf, Strictly single-site dmrg algorithm with subspace expansion, Phys. Rev. B **91**, 155115 (2015).
[90] I. P. McCulloch and M. Gulácsi, The non-Abelian density matrix renormalization group algorithm, Europhys. Lett. **57**, 852 (2002).
[91] C. Hubig, I. P. McCulloch, and U. Schollwöck, Generic construction of efficient matrix product operators, Phys. Rev. B **95**, 035129 (2017).
[92] L. Michel and I. P. McCulloch, Schur Forms of Matrix Product Operators in the Infinite Limit, arXiv:1008.4667.
[93] S. N. Saadatmand (unpublished).
[94] J. W. G. Wilder, L. C. Venema, A. G. Rinzler, R. E. Smalley, and C. Dekker, Electronic structure of atomically resolved carbon nanotubes, Nature (London) **391**, 59 (1998).
[95] F. Kolley, M. Piraud, I. P. McCulloch, U. Schollwöck, and F. Heidrich-Meisner, Strongly interacting bosons on a three-leg ladder in the presence of a homogeneous flux, New J. Phys. **17**, 092001 (2015).
[96] P. Lecheminant, B. Bernu, C. Lhuillier, and L. Pierre, J_1-J_2 quantum Heisenberg antiferromagnet on the triangular lattice: A group-symmetry analysis of order by disorder, Phys. Rev. B **52**, 6647 (1995).
[97] K. Slagle and C. Xu, Quantum phase transition between the Z_2 spin liquid and valence bond crystals on a triangular lattice, Phys. Rev. B **89**, 104418 (2014).
[98] Y.-M. Lu, Symmetric Z_2 spin liquids and their neighboring phases on triangular lattice, Phys. Rev. B **93**, 165113 (2016).
[99] H. Neuberger and T. Ziman, Finite-size effects in Heisenberg antiferromagnets, Phys. Rev. B **39**, 2608 (1989).
[100] M. B. Hastings, Lieb-Schultz-Mattis in higher dimensions, Phys. Rev. B **69**, 104431 (2004).
[101] M. B. Hastings, Locality in Quantum and Markov Dynamics on Lattices and Networks, Phys. Rev. Lett. **93**, 140402 (2004).
[102] A. Kitaev and J. Preskill, Topological Entanglement Entropy, Phys. Rev. Lett. **96**, 110404 (2006).
[103] M. Levin and X.-G. Wen, Detecting Topological Order in a Ground State Wave Function, Phys. Rev. Lett. **96**, 110405 (2006).
[104] Y. Zhang, T. Grover, and A. Vishwanath, Topological entanglement entropy of Z_2 spin liquids and lattice Laughlin states, Phys. Rev. B **84**, 075128 (2011).
[105] L. Wang, D. Poilblanc, Z.-C. Gu, X.-G. Wen, and F. Verstraete, Constructing a Gapless Spin-Liquid State for the Spin-1/2 $J_1 - J_2$ Heisenberg Model on a Square Lattice, Phys. Rev. Lett. **111**, 037202 (2013).
[106] M. A. Metlitski and T. Grover, Entanglement entropy of systems with spontaneously broken continuous symmetry, arXiv:1112.5166.
[107] H.-C. Jiang, Z. Wang, and L. Balents, Identifying topological order by entanglement entropy, Nat. Phys. **8**, 902 (2012).
[108] A. Hamma, R. Ionicioiu, and P. Zanardi, Bipartite entanglement and entropic boundary law in lattice spin systems, Phys. Rev. A **71**, 022315 (2005).
[109] A. Hamma, R. Ionicioiu, and P. Zanardi, Ground state entanglement and geometric entropy in the kitaev model, Phys. Lett. A **337**, 22 (2005).
[110] J. D. Bekenstein, Black holes and entropy, Phys. Rev. D **7**, 2333 (1973).
[111] M. Srednicki, Entropy and Area, Phys. Rev. Lett. **71**, 666 (1993).
[112] M. B. Plenio, J. Eisert, J. Dreißig, and M. Cramer, Entropy, Entanglement, and Area: Analytical Results for Harmonic Lattice Systems, Phys. Rev. Lett. **94**, 060503 (2005).
[113] S.-H. Tsai and S. R. Salinas, Fourth-order cumulants to characterize the phase transitions of a spin-1 ising model, Braz. J. Phys. **28**, 58 (1998).
[114] A. Malakis, P. Kalozoumis, and N. G. Fytas, Continious- and first-order phase transitions in ising antiferromagnets with next-nearest-neighbour interations, Rev. Adv. Mater. Sci. **14**, 1 (2007).
[115] K. Binder, Critical Properties from Monte Carlo Coarse Graining and Renormalization, Phys. Rev. Lett. **47**, 693 (1981).
[116] K. Binder, Finite size scaling analysis of ising model block distribution functions, Z. Phys. B: Condens. Matter **43**, 119 (1981).
[117] K. Binder and D. P. Landau, Finite-size scaling at first-order phase transitions, Phys. Rev. B **30**, 1477 (1984).
[118] W.-L. You, Y.-W. Li, and S.-J. Gu, Fidelity, dynamic structure factor, and susceptibility in critical phenomena, Phys. Rev. E **76**, 022101 (2007).
[119] L. Rademaker, Tower of states and the entanglement spectrum in a coplanar antiferromagnet, Phys. Rev. B **92**, 144419 (2015).
[120] M. Zaletel, Y.-M. Lu, and A. Vishwanath, Measuring space-group symmetry fractionalization in Z_2 spin liquids, arXiv:1501.01395.
[121] L. C. Biedenharn, J. D. Louck, and P. A. Carruthers, *Angular momentum in quantum physics: Theory and application*, Encyclopedia of Mathematics and its Applications (Cambridge University Press, 2009).
[122] S.-S. Gong, W. Zhu, J.-X. Zhu, D. N. Sheng, and K. Yang, Global phase diagram and quantum spin liquids in a spin-1/2 triangular antiferromagnet, Phys. Rev. B **96**, 075116 (2017).